



1 **The AICC2023 chronological framework and associated timescale**  
2 **for the EPICA Dome C ice core.**

3 **Marie Bouchet**<sup>1</sup>, Amaëlle Landais<sup>1</sup>, Antoine Grisart<sup>1</sup>, Frédéric Parrenin<sup>2</sup>, Frédéric Prié<sup>1</sup>,  
4 Roxanne Jacob<sup>1</sup>, Elise Fourré<sup>1</sup>, Emilie Capron<sup>2</sup>, Dominique Raynaud<sup>2</sup>, Vladimir Ya Lipenkov<sup>3</sup>,  
5 Marie-France Loutre<sup>4,5</sup>, Thomas Extier<sup>6</sup>, Anders Svensson<sup>7</sup>, Etienne Legrain<sup>2</sup>, Patricia  
6 Martinerie<sup>2</sup>, Markus Leuenberger<sup>8</sup>, Wei Jiang<sup>9</sup>, Florian Ritterbusch<sup>9</sup>, Zheng-Tian Lu<sup>9</sup>, Guo-Min  
7 Yang<sup>9</sup>.

8 <sup>1</sup>Laboratoire des Sciences du Climat et de l'Environnement, UMR8212, CNRS, 91190 Gif sur Yvette, France.

9 <sup>2</sup>Univ. Grenoble Alpes, CNRS, INRAE, IRD, Grenoble INP, IGE, 38000 Grenoble, France

10 <sup>3</sup>Arctic and Antarctic Research Institute, 199397 St. Petersburg, Russia.

11 <sup>4</sup>PAGES International Project Office University of Bern, 3012 Bern, Switzerland.

12 <sup>5</sup>Université catholique de Louvain, B-1348 Louvain-la-Neuve, Belgium.

13 <sup>6</sup>Univ. Bordeaux, CNRS, Bordeaux INP, EPOC, UMR 5805, 33600 Pessac, France.

14 <sup>7</sup>Niels Bohr Institute, University of Copenhagen, 2100 Copenhagen, Denmark.

15 <sup>8</sup>Physics Institute, University of Bern, 3012 Bern, Switzerland.

16 <sup>9</sup>Hefei National Laboratory, University of Science and Technology of China, Hefei, 230026, China.

17

18 *Correspondance to:* Marie Bouchet ([marie.bouchet@lsce.ipsl.fr](mailto:marie.bouchet@lsce.ipsl.fr))

19 **Abstract.** The EPICA (European Project for Ice Coring in Antarctica) Dome C (EDC) ice core drilling in East  
20 Antarctica reaches a depth of 3260 m. The reference EDC chronology (AICC2012) provides an age vs depth  
21 relationship covering the last 800 kyr (thousands of years) with an absolute uncertainty rising up to 8,000 years at  
22 the bottom of the ice core. The origins of this relatively large uncertainty are threefold: (1) the  $\delta^{18}\text{O}_{\text{atm}}$ ,  $\delta\text{O}_2/\text{N}_2$   
23 and total air content (TAC) records are poorly resolved and discontinuous over the last 800 kyr, (2) the three orbital  
24 tools are not used simultaneously and (3) large uncertainties are associated with their orbital targets. Here, we  
25 present new highly resolved  $\delta^{18}\text{O}_{\text{atm}}$ ,  $\delta\text{O}_2/\text{N}_2$  and  $\delta^{15}\text{N}$  measurements for EDC ice core covering the last five  
26 glacial - interglacial transitions as well as novel absolute  $^{81}\text{Kr}$  ages. We have compiled chronological and  
27 glaciological information including novel orbital age markers from new data on EDC ice core as well as accurate  
28 firn modeling estimates in a Bayesian dating tool to construct the new AICC2023 chronology. The average  
29 uncertainty of the ice chronology is reduced from 2,500 years to 1,800 years in AICC2023 over the last 800 kyr.  
30 The new timescale diverges from AICC2012 and suggests age shifts reaching 3,800 years towards older ages over  
31 Marine Isotopes Stages (MIS) 5, 11 and 19. But, the coherency between the new AICC2023 timescale and  
32 independent chronologies of other archives (Italian Lacustrine succession from Sulmona Basin, Dome Fuji ice  
33 core and northern Alpine speleothems) is improved by 1,000 to 2,000 years over these time intervals.

34

35

36 **1 Introduction**

37 Deep polar ice cores are unique archives of past climate and their investigation is valuable to study mechanisms  
38 governing the Earth's climate variations. Precise chronologies are key to identify the successions and lengths of



39 climatic events, along with exploring phase relationships between the external forcing (changes in the Earth's  
40 orbit) and the diverse climatic responses (variations in temperature and atmospheric greenhouse gas  
41 concentrations). To date ice cores, we need to construct two separate chronologies: one for the ice and one for the  
42 younger air trapped in bubbles. Due to the thinning of ice horizontal layers as we go down in depth, a wide timespan  
43 of paleoclimatic information is zipped within the deepest part of the ice sheet. Therefore, many of the ice core  
44 community ongoing efforts focus on improving deep ice cores timescales for ice and gas phases, as well as  
45 extending them further back in time (Crotti et al., 2021; Oyabu et al., 2022). Ice cores drilled at sites characterized  
46 by a high accumulation rate of snow at surface (10 to 30 cm/year) can be dated by counting ice layers deposited  
47 year after year (Svensson et al., 2008; Sigl et al., 2016). On the contrary, East Antarctica sites are associated with  
48 very low accumulation rates (1 to 5 cm/year) which prevent annual layers from being identified and counted. As  
49 a consequence, chronologies of ice cores at low-accumulation sites are commonly established using ice flow and  
50 accumulation models tied up with chronological and glaciological constraints (Veres et al., 2013; Bazin et al.,  
51 2013; Parrenin et al., 2017).

52 Glaciological modeling has been historically used to date Greenlandic and Antarctic ice cores. A  
53 unidimensional ice flow model was first applied to the Camp Century ice core (Dansgaard and Johnsen, 1969),  
54 and later to other ice cores such as the ones drilled at EDC and Dome Fuji (EPICA members, 2004; Parrenin et  
55 al., 2007). First, water isotopes ( $\delta D$  or  $\delta^{18}O$ ) measurements provide estimates of past evolution of the accumulation  
56 rate of snow and temperature at surface. Then, an ice flow model (Parrenin et al., 2004) takes as inputs past  
57 accumulation together with a vertical velocity depth-profile through the ice sheet to determine the thinning of  
58 annual snow/ice layers in time, and therefore the ice timescale. This approach is very sensitive to some poorly  
59 known parameters such as boundary conditions. For this reason, the glaciological modeling approach is  
60 complemented with chronological constraints (gas or ice age known at certain depth levels).

61 Chronological constraints obtained either by measurement of radionuclides or by synchronization to a  
62 curve of reference are established for both ice and gas timescales. For building long chronologies, some time  
63 constraints can be obtained from the  $^{10}Be$  series measured in ice. The  $^{10}Be$  cosmogenic nuclide is produced at  
64 different rate depending on the solar activity and its arrival on Earth is modulated by the strength of the Earth's  
65 magnetic field (Yiou et al., 1997; Raisbeck et al., 2007; Heaton et al., 2021). Some links hence exist between  $^{10}Be$   
66 flux and precisely dated magnetic events such as the Laschamp excursion, an abrupt decline in the geomagnetic  
67 field magnitude occurring at about 41 ka BP (thousand years before 1950) and visible as a positive excursion in  
68 the  $^{10}Be$  flux records in ice cores (Raisbeck et al., 2017; Lascu et al., 2016).  $^{40}Ar$  measurements in the gas phase  
69 of Antarctic ice cores also provide dating constraints for old ice, especially for non-continuous stratigraphic  
70 sequences (Yan et al., 2019).  $^{40}Ar$  is produced in solid earth by the radioactive decay of  $^{40}K$  leading to an increasing  
71 concentration of  $^{40}Ar$  in the atmosphere at a rate of  $0.066 \pm 0.006\% \text{ Myr}^{-1}$  (Bender et al., 2008). Recently, the  
72 possibility of measuring  $^{81}Kr$  in ice samples of a few kg gave a new absolute dating tool for ice cores.  $^{81}Kr$  is a  
73 radioactive isotope that is suitable for dating ice cores in the range from 0.03 to 1.3 Ma BP (million years before  
74 1950), making it perfectly adapted for Antarctic ice core dating (Crotti et al., 2021; Buizert et al., 2014).

75 To further constrain oldest ice core chronologies, the so-called "orbital dating" tools are also used. These  
76 tools consist in aligning some tracers measured in ice cores to the Earth orbital series, called targets, whose  
77 fluctuations in time are accurately calculated from the known variations of orbital parameters (Berger, 1978;  
78 Laskar et al., 2011). The synchronization of the orbital tracer with its target provides ice or gas age constraints. So



79 far, three orbital dating tools have been developed:  $\delta^{18}\text{O}$  of  $\text{O}_2$  ( $\delta^{18}\text{O}_{\text{atm}}$ ),  $\delta\text{O}_2/\text{N}_2$  and total air content (TAC).  
80  $\delta^{18}\text{O}_{\text{atm}}$  was typically aligned with the precession parameter (or with the 21<sup>st</sup> June insolation at 65°North) delayed  
81 by 5,000 years because such a lag between  $\delta^{18}\text{O}_{\text{atm}}$  and its orbital target was observed during the last deglaciation  
82 (Dreyfus et al., 2007; Shackleton, 2000). However, variations in the phasing between  $\delta^{18}\text{O}_{\text{atm}}$  and precession have  
83 been suspected (Jouzel et al., 2002) and identified since (Bazin et al., 2016), and millennial-scale events (as  
84 Heinrich-like events) occurring during deglaciations have been shown to delay the response of  $\delta^{18}\text{O}_{\text{atm}}$  to orbital  
85 forcing (Extier et al., 2018). Because there was a significant unpredictability in the lag between  $\delta^{18}\text{O}_{\text{atm}}$  and its  
86 orbital target, a large uncertainty in the  $\delta^{18}\text{O}_{\text{atm}}$  based tie points (up to 6,000 years) was assigned in the  
87 construction of AICC2012 (Bazin et al., 2013). To improve the accuracy of the gas timescale, Extier et al. (2018)  
88 rather aligned the variations of  $\delta^{18}\text{O}_{\text{atm}}$  to the  $\delta^{18}\text{O}_{\text{calcite}}$  recorded in absolute dated East Asian speleothems  
89 between 640 and 100 ka BP. Indeed, the two records show similar orbital (related to the 21<sup>st</sup> July insolation at 65°  
90 North) and millennial variabilities, which may correspond to southward shifts in the InterTropical Convergence  
91 Zone (ITCZ) position, themselves linked to Heinrich-like events as supported by the modeling study of Reutenauer  
92 et al. (2015).

93 In parallel, Bender (2002) observed that the elemental ratio  $\delta\text{O}_2/\text{N}_2$  of air trapped in Vostok ice core  
94 appears to vary in phase with the 21<sup>st</sup> of December insolation at 78° South (Vostok latitude) between 400 and 160  
95 ka BP. Subsequent observations led Bender (2002) to assert that local summer solstice insolation affects near-  
96 surface snow metamorphism and that this imprint is preserved as snow densifies in the firn and, later on, affects  
97 the ratio  $\delta\text{O}_2/\text{N}_2$  measured in air bubbles formed at the lock-in-zone. Wiggle matching between  $\delta\text{O}_2/\text{N}_2$  and local  
98 summer solstice insolation has been used to construct orbital timescales for Dome Fuji, Vostok and EDC ice cores  
99 reaching back 360, 400 and 800 ka BP respectively, with a chronological uncertainty for each  $\delta\text{O}_2/\text{N}_2$  tie point  
100 estimated between 800 and 4,000 years (Kawamura et al., 2007; Suwa & Bender, 2008; Bazin et al., 2013).  
101 Finally, Raynaud et al. (2007) found very similar spectral properties between the TAC record of EDC and the  
102 integrated summer insolation at 75°South (ISI) obtained by a summation over a year of all daily local insolation  
103 above a certain threshold over the last 440 kyr. As for  $\delta\text{O}_2/\text{N}_2$ , these similarities may be explained by the insolation  
104 imprint in near-surface snow well preserved down to the lock-in zone, where it could affect the air content in deep  
105 ice although the physical mechanisms involved during the snow and firn densification for  $\delta\text{O}_2/\text{N}_2$  and TAC are  
106 likely different (Lipenkov et al., 2011). Lately, Bazin et al. (2013) made use of TAC to constrain Vostok and EDC  
107 ice core chronologies back to 430 ka BP with an uncertainty for each TAC tie point varying between 3,000 and  
108 7,000 years. Although these three orbital tools complement each other (TAC and  $\delta\text{O}_2/\text{N}_2$  inferred ages agree  
109 within less than 1,000 years between 390 and 160 ka BP for the Vostok ice core, Lipenkov et al., 2011), they  
110 hardly ever have been employed together. Plus, they are often associated with large uncertainties (reaching 7,000  
111 years) which lie in the choice of the appropriate orbital target, in its alignment with ice core records that can be  
112 ambiguous during periods of low eccentricity in the Earth's orbit (leading to low-amplitude insolation variations)  
113 and in the poor quality of the signals measured in the deepest section of the cores.

114 To connect ice and gas timescales, the estimation of the lock-in-depth (LID), indicating the lowest depth where  
115 air is trapped in enclosed bubbles and no longer diffuses (Buizert et al., 2013), is used to calculate the ice/gas age  
116 difference. Measurements of  $\delta^{15}\text{N}$  from  $\text{N}_2$  yield a first estimate of this depth and the LID can also be calculated  
117 with firn densification modeling (Bréant et al., 2017; Goujon et al., 2003).



118 For many years, each polar ice core was characterized by its peculiar timescale which was not naturally  
119 consistent with other ice cores timescales. To address this issue, other measurements provide relative dating  
120 constraints (stratigraphic links) improving the coherency between timescales of ice cores from both hemispheres.  
121 The synchronization of globally well-mixed atmospheric methane ice core records gives tie points with an accuracy  
122 of a few decades to several centuries (60-1,500 years) (Lemieux-Dudon et al., 2010; Epifanio et al., 2020). Climate  
123 independent events, such as large volcanic eruptions, can be observed in ice cores from Greenland and Antarctica  
124 via singular patterns of the distribution of sulfate. Identification of these deposits permits to precisely synchronize  
125 several ice cores (within 5 to 150 years) (Svensson et al., 2020).

126 In order to integrate stratigraphic matching, independent synchronization and absolute dating constraints as  
127 well as glaciological modeling to produce coherent ice core chronologies, researchers developed Bayesian dating  
128 tools such as Datic (Lemieux-Dudon et al., 2010), IceChrono1 (Parrenin et al., 2015) and PaleoChrono (Parrenin  
129 et al., 2021). These tools use an inverse method combining all chronological information to provide a coherent age  
130 scale for several ice cores. These probabilistic tools adjust prior estimates of ice and gas chronologies built with a  
131 glaciological model (background scenario) so that they respect chronological constraints.

132 Here we focus on the chronology of the EDC deep ice core. The EPICA project provided two cores in  
133 East Antarctica including one at Dome C (EDC, 2004). The second (and final) drilling attempt at Dome C gave  
134 the 3260 m long EDC99 core, whose drilling has been willingly stopped at 15 m above bedrock due to expected  
135 presence of melt water. EDC furnishes the oldest continuous ice core record so far, covering the last 800 kyr  
136 (EPICA community members, 2004; Jouzel et al., 2007).

137 Bazin et al. (2013) and Veres et al. (2013) used the probabilistic dating tool Datic to establish the  
138 coherent chronology AICC2012 back to 800 ka BP for five ice cores including EDC, Vostok, EPICA Dronning  
139 Maud Land ice core (EDML), North Greenland Ice core Project (NGRIP) and Talos Dome Ice core (TALDICE).  
140 To determine EDC age scale, they used various orbital dating constraints including: 39 tie points attached to a  
141 6,000 years uncertainty derived from  $\delta^{18}\text{O}_{\text{atm}}$  tuning to 5,000 years delayed precession between 800 and 300 ka  
142 BP, 20 tie points associated with a 4,000 years uncertainty from  $\delta\text{O}_2/\text{N}_2$  alignment to local summer solstice  
143 insolation between 800 and 300 ka BP, and 14 tie points linked to an uncertainty between 3,000 and 7,000 years  
144 using TAC synchronised to integrated summer insolation between 430 and 0 ka BP. However, due to the lack of  
145 data for the orbital dating approach, AICC2012 uncertainty is of 2,500 years on average, reaching 8,000 years at  
146 the bottom of the core. The origins of AICC2012 uncertainty can be divided in the following points: (i) discrepancy  
147 between  $\delta^{18}\text{O}_{\text{atm}}$ ,  $\delta\text{O}_2/\text{N}_2$  and TAC series and their orbital target; (ii) discontinuity and poor quality of the  $\delta\text{O}_2/\text{N}_2$   
148 and TAC records; (iii) uncertainty on the phasing between  $\delta^{18}\text{O}_{\text{atm}}$  and precession; (iv) poor constraint on the LID  
149 scenario due to a disagreement between  $\delta^{15}\text{N}$  data and firn modeling estimates (Bréant et al., 2017).

150 It is now possible to address each source of uncertainty thanks to recent advances: (i) Since AICC2012,  
151 the  $\delta^{18}\text{O}_{\text{atm}}$ ,  $\delta\text{O}_2/\text{N}_2$  and TAC records have been extended, now covering the last 800 kyr (Extier et al., 2018c,  
152 b). In addition, new highly resolved  $\delta^{18}\text{O}_{\text{atm}}$  and  $\delta\text{O}_2/\text{N}_2$  measurements are available over several glacial  
153 terminations (TII, III, IV, V and VI) (Grisart, 2023). (ii) Extier et al. (2018) recently suggested a  $\delta^{18}\text{O}_{\text{atm}}$  based  
154 timescale using  $\delta^{18}\text{O}_{\text{calcite}}$  of East Asian speleothems as an alternative tuning target to precession. This choice  
155 reduces the chronological uncertainty between 640 and 100 ka BP. (iii) Finally, new highly resolved  $\delta^{15}\text{N}$  data  
156 covering the Terminations II to VI are available (Grisart, 2023). In parallel, firn densification models have been



157 progressively improved and the model described in Bréant et al. (2017) can be employed to estimate LID evolution  
158 in the past when  $\delta^{15}\text{N}$  data are still missing.

159 In this work, we implement new absolute age constraints spanning the last 800 kyr derived from  $^{81}\text{Kr}$  measured  
160 in air trapped in EDC ice core as well as new orbital age constraints obtained by synchronizing up-to-date EDC  
161 records with their orbital target. We combine these data to recent volcanic matching and methane records  
162 synchronization which provide additional stratigraphic links, relating EDC to other ice cores over the past 122 kyr  
163 (Svensson et al., 2020; Baumgartner et al., 2014). Finally, we propose the new chronology AICC2023 with reduced  
164 chronological uncertainties.

## 165 2 Methods

### 166 2.1 Dating strategy

167 The Paleochrono Python software is a probabilistic dating tool similar to Datice and Icechronol with  
168 improved mathematical, numerical and programming capacities (Parrenin et al., 2021). The dating strategy of  
169 Paleochrono relies on the Bayesian inference of three glaciological functions forming the input background  
170 scenario: accumulation rate ( $A$ ), thinning of annual ice layers ( $\tau$ ) and Lock-In-Depth ( $LID$ ). The three variables  
171 evolve along the ice core depth  $z$  and are used to estimate the ice ( $\psi$ ) and gas ( $\chi$ ) age profiles as follows:

$$172 \quad \psi(z) = \int_0^z \frac{D(z')}{\tau(z')A(z')} dz' \quad (1)$$

$$173 \quad \chi(z) = \psi(z - \Delta depth(z)) \quad (2)$$

$$174 \quad \int_{z - \Delta depth(z)}^z \frac{D(z')}{\tau(z')} dz' = LID(z) \times \frac{D}{\tau} \Big|_{firn}^0 \quad (3)$$

175 where  $D$  is the relative density of the snow/ice and  $\frac{D}{\tau} \Big|_{firn}^0$  the average value of  $\frac{D}{\tau}$  in the firn when the air particle  
176 was at the lock-in-depth (this parameter is usually  $\sim 0.7$ , Parrenin et al., 2012). The age scales are further  
177 constrained to respect chronological constraints identified from observations. To specify the credibility of the  
178 background scenario for the age scales and the chronological constraints, the glaciological functions  
179 (accumulation, thinning and LID) and the chronological information can be mathematically expressed as  
180 probability densities which are presumed to be Gaussian and independent (i.e. decorrelated between them). Thus,  
181 the inference is based on the Least Square optimisation method (implying all probability densities Gaussian). It is  
182 numerically solved using the Trust Region algorithm (assuming that the model is roughly linear around the  
183 solution) and the Jacobian of the model is evaluated analytically for an improved computation time. As a result,  
184 the best adjustment between the background scenario and chronological observations is found, providing the most  
185 probable scenario as a posterior evaluation of the three glaciological functions and hence chronologies for ice and  
186 air. For each ice core, the input files for Paleochrono are the following: (i) the background values of the three  
187 glaciological functions with depth, (ii) gas and ice stratigraphic links, (iii) gas and ice dated horizons, which are  
188 tie points derived for one core from absolute and synchronization dating methods, (iv) gas and ice intervals of



189 known durations and (v) depth difference estimates between the same event recorded in the gas and ice matrix  
190 ( $\Delta$ depth). Specific relative or absolute uncertainties are attached to each of these parameters in each input file.

191 In this study, we added numerous gas and ice dated horizons for EDC as well as an updated background  
192 scenario for the LID. Then, to construct a new chronology for EDC ice core that is consistent with the timescales  
193 of Vostok, TALDICE, EDML and NGRIP ice cores, we followed the same strategy as for the construction of  
194 AICC2012. Glaciological background parameters and dating constraints for Vostok, TALDICE, EDML, NGRIP  
195 and EDC drillings are compiled in one run of Paleochrono to obtain AICC2023. Vostok, TALDICE, EDML and  
196 NGRIP background parameters and dating constraints are extracted from Bazin et al. (2013) except for: (i) new  
197 Vostok gas age constraints determined from the alignment of  $\delta^{18}\text{O}_{\text{atm}}$  and East Asian  $\delta^{18}\text{O}_{\text{calcite}}$  records as for  
198 EDC (see supplementary Fig. S5), (ii) new TALDICE background parameters and (iii) age constraints from Crotti  
199 et al. (2021) and (iv) corrected LID background scenarios for Vostok and EDML sites (see supplementary Fig.  
200 S6). In order to prevent any confusion with reference ice core timescales, the new AICC2023 chronology for  
201 NGRIP is compelled to respect exactly the layer-counted GICC05 timescale over the last 60 kyr (Andersen et al.,  
202 2006). For this reason, we did not use the methodology described by Lemieux-Dudon et al. (2015) which  
203 implemented layer counting as a constraint on the duration of events in the dating tool, inducing a slight shift  
204 (maximum 410 years) on the AICC2012 timescale. The resulting Paleochrono experiment provides the new  
205 official chronology AICC2023 for the EDC ice core. The contingent timescales obtained for the four other sites  
206 are not the subject of this study but are also provided in the Supplementary Material.

## 207 2.2 Analytical method

### 208 2.2.1 $\delta^{18}\text{O}_{\text{atm}}$ , $\delta\text{O}_2/\text{N}_2$ and $\delta^{15}\text{N}$

209 The measurements of the isotopic and elemental compositions of  $\text{O}_2$  and  $\text{N}_2$  were performed by Grisart  
210 (2023) at LSCE following the method described by Bréant et al. (2019) and Extier et al. (2018). The air trapped in  
211 the EDC ice core is extracted using the semi-automatic line which eliminates  $\text{CO}_2$  and  $\text{H}_2\text{O}$ . 30 to 40 g samples  
212 are prepared in a cold environment ( $-20^\circ\text{C}$ ), their exterior layer (3-5mm) is removed so that there is no exchange  
213 with atmospheric air and each sample is cut in two replicates. Each day, three ice samples (and replicates) are  
214 placed in six flasks and the atmospheric air is evacuated from the flasks. Samples are then melted and left at  
215 ambient temperature for approximately 1h30 in order to extract the air trapped in ice samples. The extracted air is  
216 then cryogenically trapped within a dedicated manifold immersed in liquid helium (Bazin et al., 2016). Along the  
217 way to the cryogenic trap, the air goes through cold traps to remove  $\text{H}_2\text{O}$  and  $\text{CO}_2$ . Two additional samples  
218 containing exterior modern air are processed through the same line every day for calibration and for monitoring  
219 the analytical set-up. Lastly, the  $\delta^{15}\text{N}$ ,  $\delta^{18}\text{O}$  of  $\text{O}_2$  and  $\delta\text{O}_2/\text{N}_2$  of each sample are measured by a dual inlet Delta  
220 V plus (Thermo Electron Corporation) mass spectrometer.

221 Classical corrections are applied on the measurements (pressure imbalance, chemical slopes, as per  
222 Landais et al., 2003). In addition,  $\delta^{15}\text{N}$  data are used to get the values of atmospheric  $\delta^{18}\text{O}$  of  $\text{O}_2$  and  $\delta\text{O}_2/\text{N}_2$  after  
223 gravitational fractionation occurred in the firm, so that  $\delta^{18}\text{O}_{\text{atm}} = \delta^{18}\text{O}$  of  $\text{O}_2 - 2 \times \delta^{15}\text{N}$  and  $\delta\text{O}_2/\text{N}_{2(\text{corr})} =$   
224  $\delta\text{O}_2/\text{N}_{2(\text{raw})} - 4 \times \delta^{15}\text{N}$  (Landais et al., 2003; Bazin et al., 2016; Extier et al., 2018). Note that our samples were  
225 stored at  $-50^\circ\text{C}$  since drilling so that no correction for gas loss was applied (see Supplementary Material).



226 Existing and new EDC data are compiled in Table 1. The resulting data set pooled standard deviations  
 227 for the new measurements are of 0.006, 0.03 and 0.04 ‰ for  $\delta^{15}\text{N}$ ,  $\delta^{18}\text{O}_{\text{atm}}$  and  $\delta\text{O}_2/\text{N}_2$  respectively.

228 **Table 1. Information on isotopic and elemental compositions measured in air trapped in EDC ice core.** \*Details on  
 229 storage and measurement conditions of  $\delta\text{O}_2/\text{N}_2$  are available in the Supplementary Material.

	$\delta^{18}\text{O}_{\text{atm}}$			$\delta\text{O}_2/\text{N}_2^*$			$\delta^{15}\text{N}$		
	Depth (m)	AICC2012 gas age (ka BP)	Resolution (kyr)	Depth (m)	AICC2012 ice age (ka BP)	Resolution (kyr)	Depth (m)	AICC2012 gas age (ka BP)	Resolution (kyr)
<b>AICC2012</b>									
Bazin et al. (2013);									
Dreyfus et al. (2007, 2008, 2010);	2479 - 3260	300 - 800	1 - 1.5	2480 - 3260	300 - 800	2.5	346 - 578 1090 - 1169 1389 - 3260	11 - 27 75 - 83 100 - 800	0.35 - 0.38 1.4 2.4
Landais et al. (2012)									
Bazin et al. (2016)	1300 - 1903 2657 - 3260	90 - 160 370 - 800	1.1	1300 - 1903 2595 - 3260	93 - 163 340 - 800	2.37 2.08			
Extier et al. (2018b, 2018c)	1872 - 2665	153 - 374	0.16 - 0.7	1904 - 2562	164 - 332	2 - 2.5			
Bréant et al. (2019)							1904 - 2580	160.2 - 334.5	1.013
	1489.95 - 1832.6	108.0 - 136.3	0.333	1489.95 - 1832.6	111.4 - 148.9	0.441	1489.95 - 1832.6	108.0 - 136.3	0.333
	1995.95 - 2350.15	180.6 - 255.8	0.437	1995.95 - 2350.15	183.9 - 259.6	0.437	1995.95 - 2350.15	180.6 - 255.8	0.437
This work (Grisart, 2023)	2555.85 - 2633.4	328.3 - 346.8	0.356	2555.85 - 2633.4	330.5 - 360.6	0.579	2555.85 - 2633.4	328.3 - 346.8	0.356
	2744.5 - 2797.85	408.7 - 445.9	0.744	2744.5 - 2797.85	410.7 - 449.6	0.779	2744.5 - 2797.85	408.7 - 445.9	0.744
	2873.75 - 2910.6	508.1 - 535.6	1.375	2873.75 - 2910.6	511.3 - 539.3	1.401	2873.75 - 2910.6	508.1 - 535.6	1.375

230

### 231 2.2.2 Total Air Content

232 The TAC record has been measured in the entire EDC ice core at the IGE following the barometric method  
 233 firstly described by Lipenkov et al. (1995). The TAC record measured in the younger part of the core (400 – 0 ka  
 234 BP) has been published in Raynaud et al. (2007) (Table 2). TAC estimates need to be corrected for cut-bubble  
 235 effect. After correction, the uncertainty in TAC values is of about 1% and the analysis replicability is better than  
 236 1%.

237

238



239 **Table 2. Information on TAC measurements.**

	TAC		
	Depth (m)	AICC2012 ice age (ka BP)	Resolution (kyr)
<b>AICC2012</b>			
(Raynaud et al., 2007)	115 - 2800	0 - 440	2.000
<i>Unpublished</i>	2800 - 3260	440 - 800	2.000

240

241

242 **2.2.3 <sup>81</sup>Kr extraction and analysis**

243 The analytical method is the same as described by Crotti et al. (2021). Three ice samples of 6 kg each are  
 244 taken from the bottom part of EDC and a slight shaving (1 mm) of the external layer is performed before  
 245 processing. The air extraction is performed through a manual extraction line following the protocol described in  
 246 Tian et al. (2019). The ice sample is placed in a 40 L stainless-steel chamber. The atmospheric air is pumped while  
 247 the chamber is kept at -20°C. The air is then slowly extracted, passing through a water trap, and compressed in a  
 248 stainless-steel cylinder. The three cylinders are sent to the University of Sciences and Technology of China (USTC,  
 249 Hefei, China) for Krypton extraction and analysis. Krypton extraction is performed after the methodology of Dong  
 250 et al. (2019) who set up an automated system for dual separation of Argon and Krypton, composed of a Titanium  
 251 getter module followed by a Gas-Chromatography separator module. The extracted Krypton is analyzed by the  
 252 Atom Trap Trace Analysis (ATTA) instrument set up at the Laser Laboratory for Trace Analysis and Precision  
 253 Measurement (LLTAPM, USTC, Hefei, China), giving the <sup>81</sup>Kr abundance R<sub>81</sub> in the sample. R<sub>81</sub> is determined  
 254 by the number of counted <sup>81</sup>Kr atoms in the sample as compared to the atmospheric reference. The anthropogenic  
 255 <sup>85</sup>Kr is measured simultaneously with <sup>81</sup>Kr to control any present-day air contamination. Here, the <sup>85</sup>Kr abundance  
 256 measured in ice samples is inferior to the detection limit, so contamination has occurred.

257 From the <sup>81</sup>Kr abundance, it is possible to estimate <sup>81</sup>Kr radioactive decay and to calculate the ice samples  
 258 age. As a noble gas isotope, <sup>81</sup>Kr is globally mixed in the atmosphere and its decay cannot be affected by complex  
 259 chemical reactions (Lu et al., 2014). <sup>81</sup>Kr half-life ( $t_{1/2}$ ) is estimated to  $\approx 229 \pm 11$  kyr (Baglin, 2008). <sup>81</sup>Kr age  
 260 can be calculated as per the following equation:

261 
$$\text{age} = -\frac{t_{1/2}}{\ln(2)} \times \ln(R_{81}) \quad (4)$$

262 The atmospheric abundance of <sup>81</sup>Kr is not constant in the past and its value is corrected using reconstruction of the  
 263 geomagnetic field intensity (Zappala et al., 2020). The error in <sup>81</sup>Kr age estimates is estimated from the statistical  
 264 error of atom counting, from the uncertainty in <sup>81</sup>Kr half-life (inducing a systematic age error) and from the size  
 265 of the sample (larger sample resulting in a smaller uncertainty).

266





267 **2.3 Firn model**

268 Firn densification models have been progressively improved over the years. While these models generally  
 269 explain well the evolution of  $\delta^{15}\text{N}$  in time through changes in the LID, they fail to reproduce values of  $\delta^{15}\text{N}$  in  
 270 some regions including coastal areas (Capron et al., 2013) and cold and low accumulation sites such as EDC. This  
 271 disagreement can be explained by an inaccurate estimate of glacial temperature and accumulation rate at surface  
 272 (Buizert et al., 2021) and/or by the impossibility to tune empirical firn models to sites with no present-day  
 273 equivalent in terms of temperature and accumulation rate (Dreyfus et al., 2010; Capron et al., 2013). Lately, the  
 274 firn model described in Bréant et al. (2017) has been developed from the IGE (Institute of Environmental  
 275 Geosciences) model (Barnola et al., 1991; Pimienta & Duval, 1987; Arnaud et al., 2000; Goujon et al., 2003)  
 276 by implementing a dependency of the firn densification rate on temperature and impurities. The temperature  
 277 dependence is added on the classical formulation of the densification rate following an Arrhenius law with an  
 278 activation energy  $Q$  as per  $\exp(-Q/RT)$  with  $R$  the perfect gas constant and  $T$  the firn temperature. Rather than  
 279 using a constant activation energy (Goujon et al., 2003), Bréant et al. (2017) stated that the value of the activation  
 280 energy should be contingent on the firn temperature value as observed in material science where the temperature  
 281 dependency exhibits the predominance of one physical mechanism among others for a material compaction at  
 282 specific temperature. Through several sensitivity tests, Bréant et al. (2017) adjusted three values for activation  
 283 energy on three different temperature ranges to reproduce best the  $\delta^{15}\text{N}$  evolution over the last deglaciation at East  
 284 Antarctic sites. The firn model also considers that firn densification is facilitated by the dissolution of impurities  
 285 within the snow (Freitag et al., 2013). If the impurity content in snow (i.e. concentration of calcium ions) is superior  
 286 to a certain threshold, the densification rate dependency to impurities is traduced by a relationship between the  
 287 new activation energy  $Q'$  and the concentration of calcium ions  $[Ca^{2+}]$ :  $Q' = f_1 \times (1 - \beta \ln(\frac{[Ca^{2+}]}{[Ca^{2+}]_{threshold}})) \times Q$   
 288 (Freitag et al., 2013). Bréant et al. (2017) assumed the impurity effect equal for all physical mechanisms and tuned  
 289  $\beta$  and  $f_1$  constants so that the modelled -  $\delta^{15}\text{N}$  data mismatch is minimized over the last glacial termination at cold  
 290 East Antarctic sites.

291 As a consequence, and in addition to our new extensive  $\delta^{15}\text{N}$  dataset, we have chosen to use here the firn  
 292 model approach of Bréant et al. (2017). In order to make a correct calculation of uncertainties linked to firn  
 293 modeling at EDC, we ran two tests of the model with and without including the impurity concentration parameter  
 294 (Table 3).

295 **Table 3. Information about the two runs of the model.**

Parameter	Test 1	Test 2
Activation energy $Q$ (densification rate)	$Q$ depending on temperature (Bréant et al., 2017)	$Q$ depending on temperature (Bréant et al., 2017)
Impurity inclusion	Yes	No

296

297 The firn densification model takes as input scenarios of temperature and accumulation rate at the surface. It  
 298 computes both the LID and the thermal gradient in the firn ( $\Delta T$ ), and then deduces the  $\delta^{15}\text{N}_{\text{therm}} = \Omega \cdot \Delta T$  with  $\Omega$



299 the thermal fractionation coefficient (Grachev and Severinghaus, 2003). The final  $\delta^{15}\text{N}$  is calculated as  $\delta^{15}\text{N} =$   
 300  $\delta^{15}\text{N}_{\text{grav}} + \delta^{15}\text{N}_{\text{therm}}$  and  $\delta^{15}\text{N}_{\text{grav}} \approx LID \cdot \frac{g}{RT}$  (first order approximation) with  $g$  the gravitational acceleration  
 301 ( $9.8 \text{ ms}^{-2}$ ),  $R$  the gas constant ( $8.314 \text{ Jmol}^{-1}\text{K}^{-1}$ ) and  $T$  the mean firn temperature (K).

### 302 3 Results

#### 303 3.1 $^{81}\text{Kr}$ age constraints

304 Three ice samples from the bottom part of EDC have been analyzed and provide three age estimates displayed  
 305 in Table 4: 629, 788 and 887 ka BP with statistical age uncertainties between 30 and 50 kyr, and a 4.8 % systematic  
 306 error due to the uncertainty in the half-life of  $^{81}\text{Kr}$ . The deepest sample suggests the presence of ice older than 800  
 307 ka BP below the 3200 m depth level and further dating studies would be valuable in exploring whether the  
 308 stratigraphy of EDC lowermost section is continuous, although this is beyond the scope of this work.

309 **Table 4. Ice samples details and radio krypton dating results.** Reported errors are 1- $\sigma$  errors. Upper limits have a 90%  
 310 confidence level. The average  $^{85}\text{Kr}$  activity in the northern hemisphere is about 75 dpm/cc in 2017. The measured  $^{85}\text{Kr}$   
 311 concentrations are inferior to the detection limit, verifying that no relevant contamination with modern air has occurred. In  
 312 addition to the statistical error on the  $^{81}\text{Kr}$  age from atom counting, a systematic error due to the uncertainty in the half-life of  
 313  $^{81}\text{Kr}$  is considered. This error would shift the calculated  $^{81}\text{Kr}$  ages up or down for all ice samples. <sup>a</sup>dpm/cc = decays per minute  
 314 per cubic centimeter STP of krypton (conversion: 100 dpm/cc corresponds to  $^{85}\text{Kr}/\text{Kr} = 3.03 \times 10^{11}$ ). <sup>b</sup>pMKr = percent Modern  
 315 Krypton (Jiang et al., 2023).

Depth (m)	Air extracted/ Ice weight (mL/kg)	Sample Used ( $\mu\text{L STP}$ , Kr)	Analysis Date	$^{85}\text{Kr}$ (dpm/cc) <sup>a</sup>	$^{81}\text{Kr}$ (pMKr) <sup>b</sup>	$^{81}\text{Kr}$ – age (ka BP) $\text{age}_{-\text{stat}-\text{sys}}^{+\text{stat}+\text{sys}}$
3013-3024	440/6.0	~0.46	18 Dec 2019	< 0.77	15.1 <sup>+1.4</sup> <sub>-1.4</sub>	629 <sup>+34+31</sup> <sub>-29-31</sub>
3144-3161	600/8.4	~0.67	30 Dec 2019	< 0.67	9.6 <sup>+1.0</sup> <sub>-1.0</sub>	788 <sup>+36+38</sup> <sub>-33-38</sub>
3216-3225	415/6.4	~0.43	16 Jan 2020	< 1.17	7.1 <sup>+1.0</sup> <sub>-1.0</sub>	887 <sup>+51+43</sup> <sub>-44-43</sub>

316

#### 317 3.2 Determination of orbital age constraints using new data

##### 318 3.2.1 $\delta\text{O}_2/\text{N}_2$

319 In this work, new highly resolved  $\delta\text{O}_2/\text{N}_2$  data on EDC ice core are presented over Terminations II, III, IV,  
 320 V and VI (Fig. 1). As these novel  $\delta\text{O}_2/\text{N}_2$  measurements have been performed on ice samples stored at  $-50^\circ\text{C}$ ,  
 321 there is no storage effect and they can directly be merged with the 800 kyr long record of Extier et al. (2018c)  
 322 (Table 1). The new dataset improves the resolution of the long EDC record, reaching sub-millennial scale accuracy  
 323 over MIS 5, 7, 9 and in particular over MIS 11 and MIS 13, periods of sparsity in the ancient record (Extier et al.,  
 324 2018c). Although the two datasets agree well over recent periods (last 350 kyr), they show some discrepancies  
 325 during older periods (between 550 and 375 ka BP, see Fig. 1). Such dissimilarities are observed over MIS 11  
 326 (between 424 and 374 ka BP) where the sampling resolution of the previous dataset is particularly low (2,500  
 327 years). In addition, the MIS 11 is a period characterised by a low eccentricity in the Earth orbit, inducing subdued  
 328 variations of insolation, causing  $\delta\text{O}_2/\text{N}_2$  changes of smaller magnitude and leading to lower signal to noise ratio.  
 329 Data by Landais et al. (2012) (shown by purple squares on Fig. 1 and S2) are consistent with the highly resolved

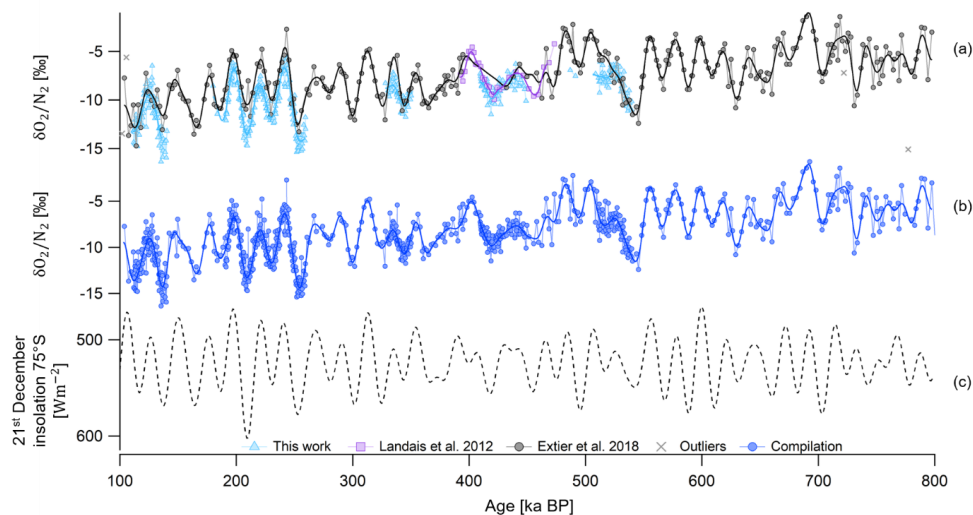


330 data presented here, supporting the relevance of the new dataset over this period. Over Termination VI (from 550  
 331 to 510 ka BP), the old dataset continuously increases while the novel dataset shows a brief maximum at around  
 332 525 ka BP followed by a minimum at around 520 ka BP. These newly revealed variations seem in phase with  
 333 insolation variations, suggesting that the new dataset shows an improved agreement with insolation. Still, highly  
 334 resolved measurements are needed in the lowermost part of the ice core where noise is significantly altering the  
 335 temporal signal.

336

337 Following a data processing treatment consistent with the method described in Kawamura et al. (2007), the  
 338 compiled dataset is linearly interpolated every 100 years, and then smoothed using a finite-duration impulse  
 339 response (FIR) filter with a KaiserBessel20 window (cut-off from 16.7 to 10.0 kyr period, number of coefficients  
 340 of 559 for the 800 kyr long record) designed with the software Igor Pro, in order to reject periods inferior to 10,000  
 341 years and erase the noise present in the data. Note that using a low-pass (rejecting periods below 15 kyr) or a band-  
 342 pass filter (keeping periods between 100 and 15 kyr periods, used by Bazin et al. (2013)) does not alter the peak  
 343 positions in the  $\delta O_2/N_2$  curve (see supplementary Fig. S1). The noise is particularly significant for highly resolved  
 344  $\delta O_2/N_2$  data and without preliminary filtering, it becomes ambiguous to identify the exact peak position (which  
 345 needs to be subjectively placed on a 1,000 to 2,000 years interval, see Supplementary Material).

346 The filter is then applied to the local summer solstice insolation curve to check that it does not induce the shift  
 347 of extrema positions by more than 100 years. This condition is verified over the last 800 kyr, except for the peaks  
 348 located at the endpoints of the record (respectively around 107 and 788 ka BP) which are then not used for tie  
 349 points determination. Outliers in the raw  $\delta O_2/N_2$  dataset are discarded if they show an anomaly superior to 3.2 ‰  
 350 when compared to the low-pass filtered signal. Five outliers are rejected out of 294 points. The  $\delta O_2/N_2$  is  
 351 interpolated and filtered again after removal of the outliers.



352 **Figure 1. Evolution of EDC  $\delta O_2/N_2$  record between 800 and 100 ka BP.** (a) EDC raw  $\delta O_2/N_2$  old data between 800 and  
 353 100 ka BP on AICC2012 ice timescale (black circles for data of Extier et al. (2018c) and purple squares for data of Landais et  
 354 al. (2012)), outliers (grey crosses) and filtered signal (black and purple lines). EDC raw  $\delta O_2/N_2$  new data (blue triangles, this  
 355 study) and filtered signals (blue line). (b) Compilation of the two datasets and filtered compiled signal. (c) 21<sup>st</sup> December

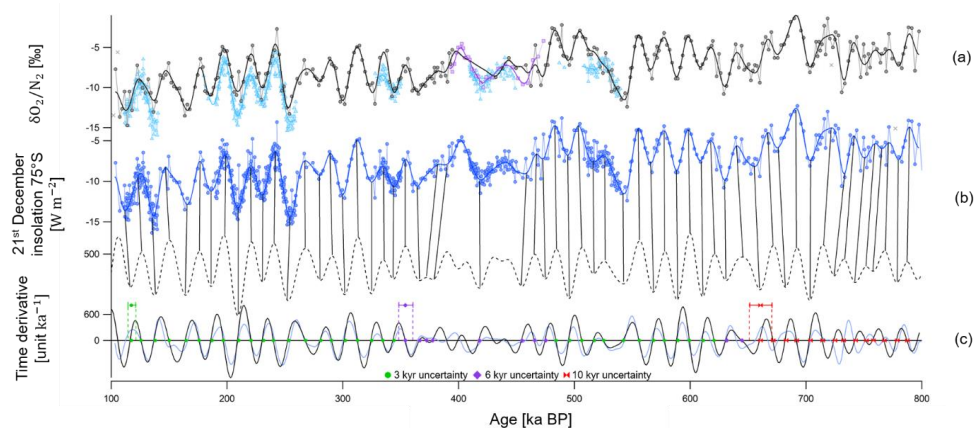


356 insolation at 75° South on a reversed axis. Zooms between 270 and 100 ka BP and between 570 and 300 ka BP are shown in  
 357 supplementary Fig. S1.

358

359 The orbital target chosen is the 21<sup>st</sup> December insolation at 75° South, which is calculated every 100 years  
 360 over the last 800 kyr (Laskar et al., 2004). The peak positions in the filtered  $\delta O_2/N_2$  compiled signal and in the  
 361 summer solstice insolation are detected via an automated method using the zero values of the time derivatives of  
 362 the  $\delta O_2/N_2$  and its orbital target. Each  $\delta O_2/N_2$  maximum is matched to an insolation minimum and each  $\delta O_2/N_2$   
 363 minimum to an insolation maximum. The data treatment and tie point identification method used here are  
 364 consistent with the approach recently performed by Oyabu et al. (2022) on a novel 207 kyr long  $\delta O_2/N_2$  record of  
 365 DF ice core.

366 Some periods, such as the MIS 11 (between 450 and 350 ka BP) and older ages (before 600 ka BP), are  
 367 characterized by a poor resemblance between the signal and the target. For instance, two or three peaks in the  
 368 insolation curve only correspond respectively to one or two peaks in the  $\delta O_2/N_2$  data. This could be explained by  
 369 a low eccentricity-induced subdued variability in the insolation target and hence in  $\delta O_2/N_2$  signal over MIS 11  
 370 and to the poor resolution of the  $\delta O_2/N_2$  measurements before 600 ka BP. In such cases, the uncertainty associated  
 371 with each tie point is ranging from 6 to 10 kyr (precession half period) and some tie points are even discarded (5  
 372 points over MIS 11 out of 63 over the last 800 kyr). Otherwise,  $\delta O_2/N_2$  seems to evolve in phase with the inverse  
 373 summer solstice insolation variations and the tie points uncertainty is set at 3 kyr. This 3 kyr uncertainty was  
 374 evaluated by Bazin et al. (2016) after having combined the three  $\delta O_2/N_2$  records from Vostok, Dome Fuji and  
 375 EDC ice cores. The orbital tuning results in 58 new tie points over the last 800 kyr (displayed in Fig. 2 and compiled  
 376 in supplementary Table S1), replacing the 20 tie points used to constrain AICC2012 between 800 and 300 ka BP  
 377 that were derived from synchronising mid-slopes of band-pass filtered  $\delta O_2/N_2$  with the insolation (Bazin et al.,  
 378 2013).



379 **Figure 2. Alignment of  $\delta O_2/N_2$  and insolation between 800 and 100 ka BP.** Extrema in the compiled filtered  $\delta O_2/N_2$   
 380 dataset (blue plain line, in panel a) are identified and matched to extrema in 21<sup>st</sup> December insolation at 75° S (dash line in panel  
 381 b). The matching peaks are linked by black vertical bars. The 0 value in the time derivative of insolation (black line in panel c)  
 382 and of the filtered  $\delta O_2/N_2$  dataset (blue line, c) corresponds to extreme values in the signals. The determined tie points between  
 383  $\delta O_2/N_2$  and insolation are depicted by markers on the bottom line. Green circles are attached to a 3 kyr uncertainty (green  
 384 horizontal error-bar represented at 117.4 ka BP), purple squares are associated with a 6 kyr uncertainty (purple horizontal



385 error-bar represented at 354.1 ka BP) and red markers with a 10 kyr uncertainty (red horizontal error-bar represented at 660.7  
386 ka BP). Between 390 and 475 ka BP, all extrema are not tuned to the target due to the poor resemblance between the signal  
387 and insolation.  
388

389 The uncertainty arising from the filter used and from the tie point identification method can be estimated  
390 by a comparison of the  $\delta\text{O}_2/\text{N}_2$  peak positions identified before and after filtering of the signal with two different  
391 methods (supplementary Fig. S2 and Table S2). The resulting uncertainty is of 700 years on average (with a  
392 standard deviation of 250 years), reaching 2,100 years around 230 ka BP.

393 The new highly resolved data presented here enable a better description of the signal variability and a  
394 reduction of the uncertainty associated with orbital tie points.

### 395 3.2.2 Total Air Content

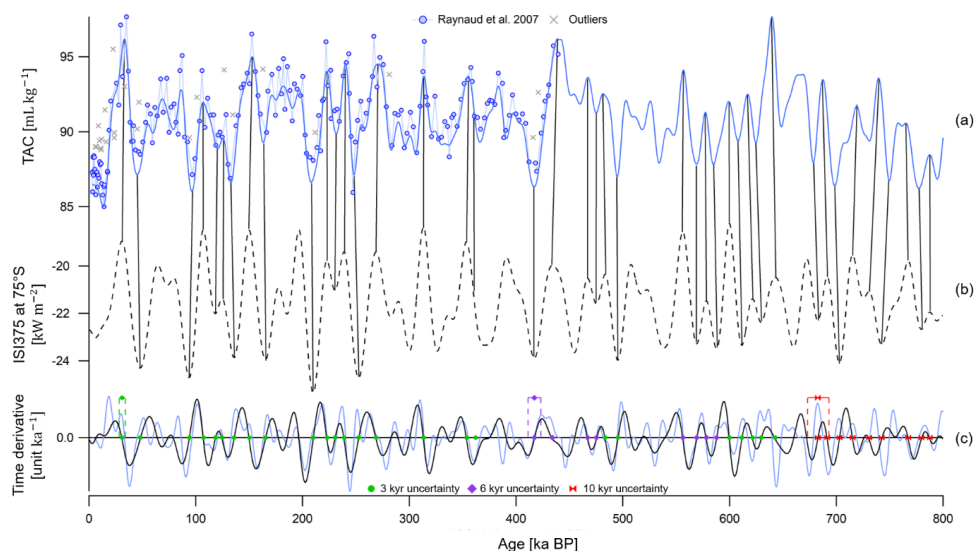
396 The new TAC record is continuous over the last 800 kyr with a mean sampling resolution of 2,000 years  
397 (Fig. 3). The raw data between 800 and 440 ka BP are not shown here and will be published in a separate study  
398 (Capron et al., in prep). The TAC series shows a good resemblance with the integrated summer insolation (ISI,  
399 obtained by a summation over a year of all daily insolation at 75° South above a chosen threshold). After  
400 comparison in the frequency domain of the TAC record of EDC ice core with ISI obtained using different  
401 thresholds, the ISI curve calculated for a threshold of 375  $\text{Wm}^{-2}$  (ISI375) exhibits the finest spectral agreement  
402 with the TAC record of EDC ice core over the past 800 kyr. The coherency between the TAC record and ISI is  
403 deficient over MIS 11 (between 430 and 370 ka BP) and in the deepest part of the core (prior to 700 ka BP) where  
404 the signal to noise ratio is low.

405 Following a data processing treatment consistent with the method described by Lipenkov et al. (2011),  
406 the 800 kyr long TAC dataset is interpolated every 100 years, and then filtered with a band-pass filter rejecting  
407 periods below 15,000 and above 46,000 years (IgorPro FIR filter with a KaiserBessel20 window: cut-off from 15  
408 to 14 kyr period and from 46 to 47 kyr period, number of coefficients of 559). Outliers in the raw TAC dataset are  
409 discarded if they show an anomaly superior to 1.0 mL/kg (standard deviation of TAC record) when compared to  
410 the band-pass filtered signal. 45 outliers are rejected out of 399 datapoints (among which 16 outliers are identified  
411 between 100 and 0 ka BP). The TAC is interpolated and filtered again after removal of the outliers.

412 Tie points are mostly determined by matching variations extrema of TAC and integrated summer  
413 insolation at 75°S (see Fig. 3). Indeed, in case of a non-linear relationship between TAC and insolation, extrema  
414 are better indicators of TAC response to insolation forcing. Moreover, filtering the dataset induces a bias in the  
415 mid-slope position. The method employed to determine extrema position is the same as for  $\delta\text{O}_2/\text{N}_2$  insolation tie  
416 points. Only one of the tie points is identified by matching mid-slopes (i.e. derivative extremum) at 362 ka BP  
417 rather than minima at 375 ka BP due to the flatness of the insolation minimum which precludes to identify an  
418 accurate tie point. All extrema are not tuned to the target due to the poor resemblance between the signal and  
419 insolation and 42 unambiguous tie points were kept out of 64 detected by the automated method. The tie point  
420 uncertainty finds its origin in the age errors associated with the filtering (~700 years), tie point identification and  
421 outlier rejection (~900 years). It is evaluated to be 3 kyr when there are good agreements: (i) between the signal  
422 and its target, meaning that one peak in ISI375 is reflected by a singular peak in the TAC record, and (ii) between  
423 the tie points identified by the automated method and manually (age shift < 1,300 years, average value) (see green  
424 circles, Fig. 3). A 6 kyr uncertainty is attached to the tie points if the latter condition is not respected (age shift >



425 1,300 years) (see purple squares, Fig. 3) and a 10 kyr uncertainty (precession half period) is inferred to the tie  
 426 points if the ISI375 variations are not reflected by the TAC record, meaning that one peak in ISI375 could be  
 427 associated with two peaks in the TAC record, or if the signal to noise ratio of the TAC record is too large (see red  
 428 markers, Fig. 3). The choices of filter and orbital target have no significant impact on the chronological uncertainty,  
 429 a further detailed study is thus beyond the scope of this work.



430 **Figure 3. Alignment of TAC and insolation between 800 and 0 ka BP.** (a) EDC raw TAC data (blue circles, Raynaud et al.  
 431 2007), outliers (grey crosses) and filtered signal (blue line) on AICC2012 ice timescale. The raw data between 800 and 440 ka BP  
 432 are not shown here and will be published in a separate study (Capron et al., in prep). (b) ISI375 at 75°S on a reversed axis.  
 433 The matching peaks and mid-slopes are linked by vertical bars. (c) Time derivative of insolation (black line) and TAC (blue  
 434 line). Its 0 value corresponds to extreme values in insolation and TAC. The determined tie points between TAC and insolation  
 435 are depicted by markers on the bottom line. Green circles are attached to a 3 kyr uncertainty (green horizontal error-bar  
 436 represented at 31 ka BP), purple squares are associated with a 6 kyr uncertainty (purple horizontal error-bar represented at 417  
 437 ka BP) and red markers with a 10 kyr uncertainty (red horizontal error-bar represented at 683 ka BP).

438

439 The orbital tuning results in 42 new tie points over the last 800 kyr (displayed in Fig. 3 and compiled in Table  
 440 S1). They replace the 14 tie points used to constrain EDC ice timescale in AICC2012 between 425 and 0 ka BP,  
 441 that were derived by direct matching mid-slope variations of unfiltered TAC and ISI target and attached to an  
 442 uncertainty varying between 2.9 and 7.2 kyr.

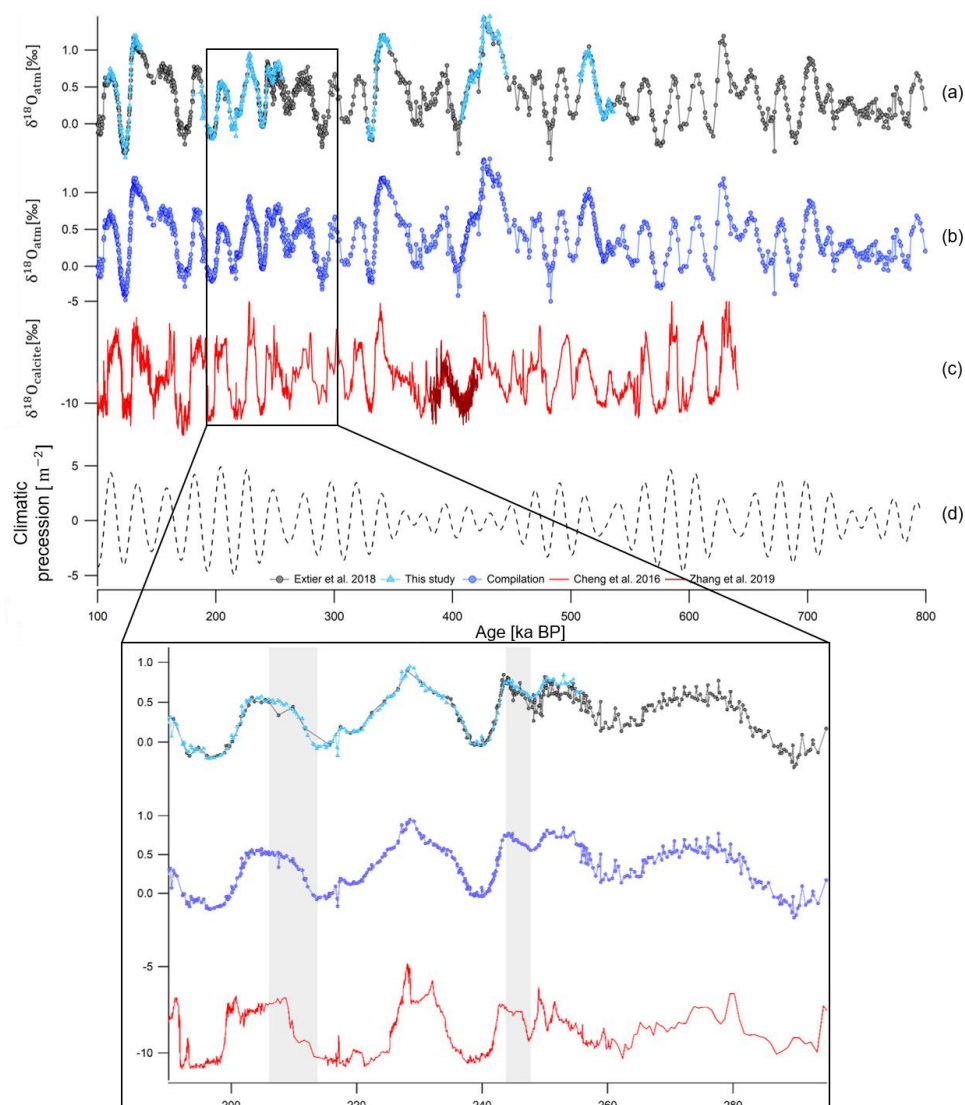
443

### 444 3.2.3 $\delta^{18}\text{O}_{\text{atm}}$

445 In this work, new highly resolved  $\delta^{18}\text{O}_{\text{atm}}$  data on EDC ice core are presented over Terminations II, III, IV,  
 446 V and VI (Fig. 4). The available  $\delta^{18}\text{O}_{\text{atm}}$  data can be sorted out in two groups: new  $\delta^{18}\text{O}_{\text{atm}}$  data (Grisart, 2023)  
 447 at high temporal resolution (between 333 and 1,375 years, see Table 1) and old measurements compiled by Extier  
 448 et al. (2018b), characterised by a lower sampling resolution (between 1,000 and 1,500 years, see Table 1), except  
 449 between 374 and 153 ka BP (resolution between 160 and 700 years, see Table 1). The new dataset allows us to  
 450 improve the resolution of the long EDC record over MIS 5, 7, 9 and in particular over MIS 11 and 13, periods of



451 sparsity in the ancient record (Extier et al., 2018b). Although the two datasets agree globally well over the last 800  
 452 kyr, the new highly resolved dataset refines the signal between 255.5 and 243 ka BP where a lot of noise is present  
 453 in the record of Extier et al. (2018b) (see inset in Fig. 4). This noise may be explained by the fact that highly  
 454 resolved (mean sampling resolution of 381 years) measurements were performed on ice samples stored at  $-20^{\circ}\text{C}$   
 455 in the compilation by Extier et al. (2018b) while the new measurements are performed on ice stored at  $-50^{\circ}\text{C}$ .  
 456 Therefore, we chose to remove the noisy dataset of Extier et al. (2018b) between 255.5 and 243 ka BP before  
 457 combining the novel dataset with the remaining 800 kyr long record of Extier et al. (2018b).



458

459 **Figure 4. Evolution of EDC  $\delta^{18}\text{O}_{\text{atm}}$  record between 800 and 100 ka BP.** (a) EDC  $\delta^{18}\text{O}_{\text{atm}}$  raw old data (black circles,  
 460 Extier et al., 2018b) and EDC  $\delta^{18}\text{O}_{\text{atm}}$  raw new data (blue triangles, Grisart, 2023) on AICC2012 gas timescale. (b)  
 461 Compilation of the two datasets after removal of old measurements between 255.5 and 243 ka BP. (c)  $\delta^{18}\text{O}_{\text{calcite}}$  composite

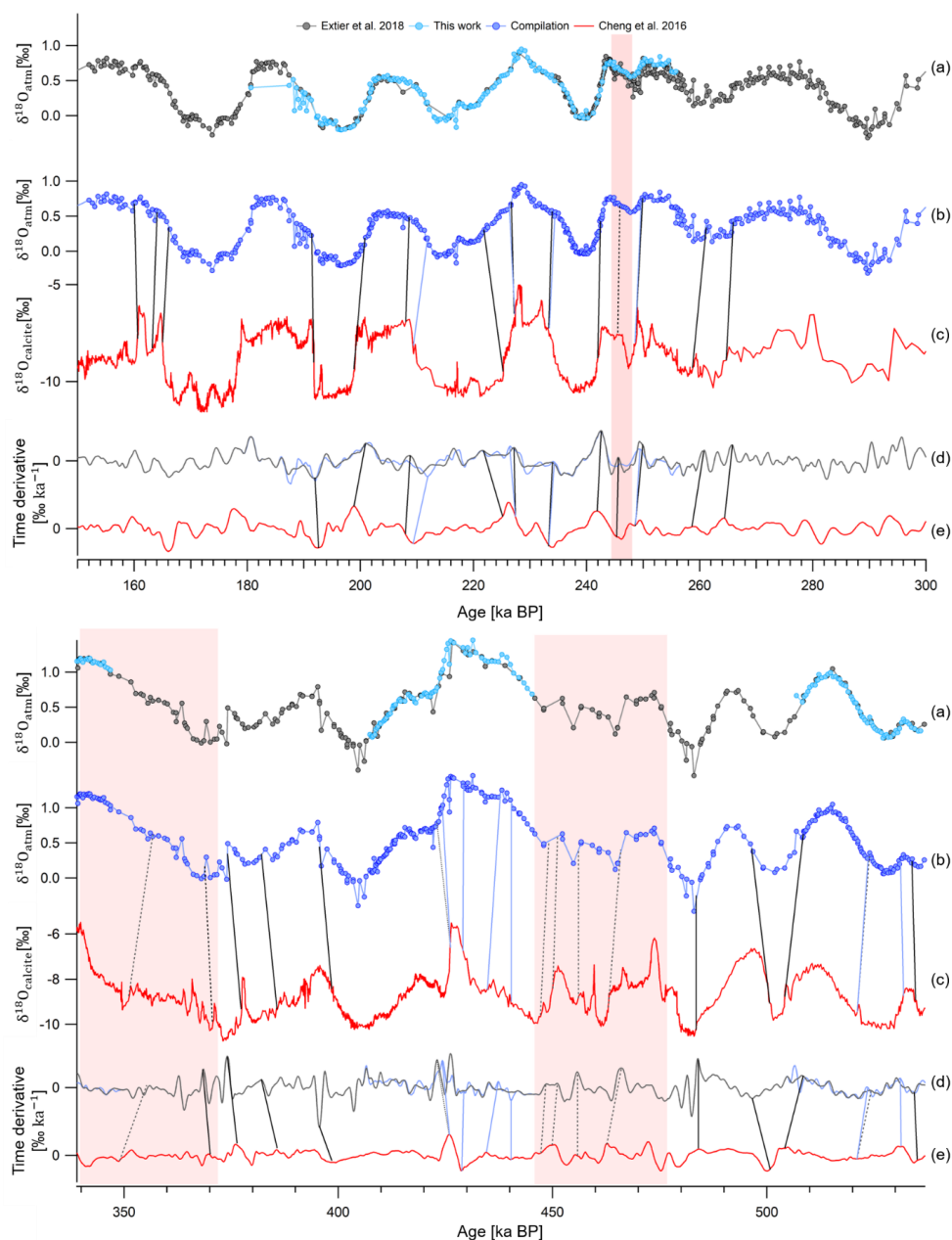


462 record from speleothems from Sambao, Dongge, Hulu (red line) and Yongxing (brown line) caves (Zhao et al., 2019; Cheng  
463 et al., 2016). (d) Climatic precession from Laskar et al. (2004) delayed by 5,000 years. Inset is a zoom between 295 and 190  
464 ka BP. Grey vertical bars highlight the improved agreement between new data of Grisart (2023) (blue triangles) and  $\delta^{18}\text{O}_{\text{calcite}}$   
465 (red line) than between old data (grey circles) and  $\delta^{18}\text{O}_{\text{calcite}}$ .

466

467 Following the dating approach proposed by Extier et al. (2018),  $\delta^{18}\text{O}_{\text{atm}}$  and  $\delta^{18}\text{O}_{\text{calcite}}$  are aligned using  
468 mid-slopes of their variations over the last 640 kyr. To do so, the compiled EDC  $\delta^{18}\text{O}_{\text{atm}}$  record and the Chinese  
469  $\delta^{18}\text{O}_{\text{calcite}}$  signal are linearly interpolated every 100 years, smoothed (25 points Savitzky-Golay) and extrema in  
470 their temporal derivative are aligned. It should be specified that synchronising  $\delta^{18}\text{O}_{\text{atm}}$  and East Asian  $\delta^{18}\text{O}_{\text{calcite}}$   
471 is not always obvious due to the long residence time of oxygen in the atmosphere (1-2 kyr) which may not be  
472 compatible with  $\delta^{18}\text{O}_{\text{calcite}}$  abrupt variations over glacial inceptions and terminations. In particular, the slow  
473 increase of the  $\delta^{18}\text{O}_{\text{atm}}$  record from 370 to 340 ka BP does not resemble the evolution of  $\delta^{18}\text{O}_{\text{calcite}}$  which is first  
474 moderate then abrupt over the same period (Fig. 5, red area). For this reason, we chose not to use the two tie points  
475 identified by Extier et al. (2018) at 351 and 370.6 ka BP. The new highly resolved data enable to identify five new  
476 tie points and to shift five tie points that have been determined beforehand by Extier et al. (2018) (Fig. 5). Between  
477 248 and 244 ka BP, the new  $\delta^{18}\text{O}_{\text{atm}}$  measurements do not coincide with the  $\delta^{18}\text{O}_{\text{calcite}}$  variations and we decided  
478 to remove the tie point identified by Extier et al. (2018) at 245.4 ka BP (Figure 5, red area). Between 480 and 447  
479 ka BP, the  $\delta^{18}\text{O}_{\text{atm}}$  variations are characterized by a low resolution (1.1 kyr) and a weak amplitude, which prevents  
480 unambiguous matching of  $\delta^{18}\text{O}_{\text{atm}}$  and  $\delta^{18}\text{O}_{\text{calcite}}$ . The four tie points identified by Extier et al. (2018) at 447.3,  
481 449.9, 455.9 and 462.8 ka BP are thus rejected (Fig. 5, red area). The remaining 39 tie points defined by Extier et  
482 al. (2018) are preserved and used here to constrain EDC gas age. Their uncertainty varies between 1.1 and 7.4 kyr.





483 **Figure 5. Alignment of EDC  $\delta^{18}\text{O}_{\text{atm}}$  and Chinese  $\delta^{18}\text{O}_{\text{calcite}}$  records over time periods where new tie points are**  
 484 **defined.** (a) EDC  $\delta^{18}\text{O}_{\text{atm}}$  new and old datasets. (b) Compiled EDC  $\delta^{18}\text{O}_{\text{atm}}$ . (c) Chinese  $\delta^{18}\text{O}_{\text{calcite}}$ . (d) Temporal derivatives  
 485 of compiled EDC  $\delta^{18}\text{O}_{\text{atm}}$  (blue curve) and of the old  $\delta^{18}\text{O}_{\text{atm}}$  dataset (black curve). (e) Temporal derivative of Chinese  
 486  $\delta^{18}\text{O}_{\text{calcite}}$  (red curve). Extrema in temporal derivatives are aligned. New tie points are represented by blue vertical bars and  
 487 tie points determined by Extier et al. (2018) and used in the new AICC2023 chronology by black vertical bars. Dotted vertical



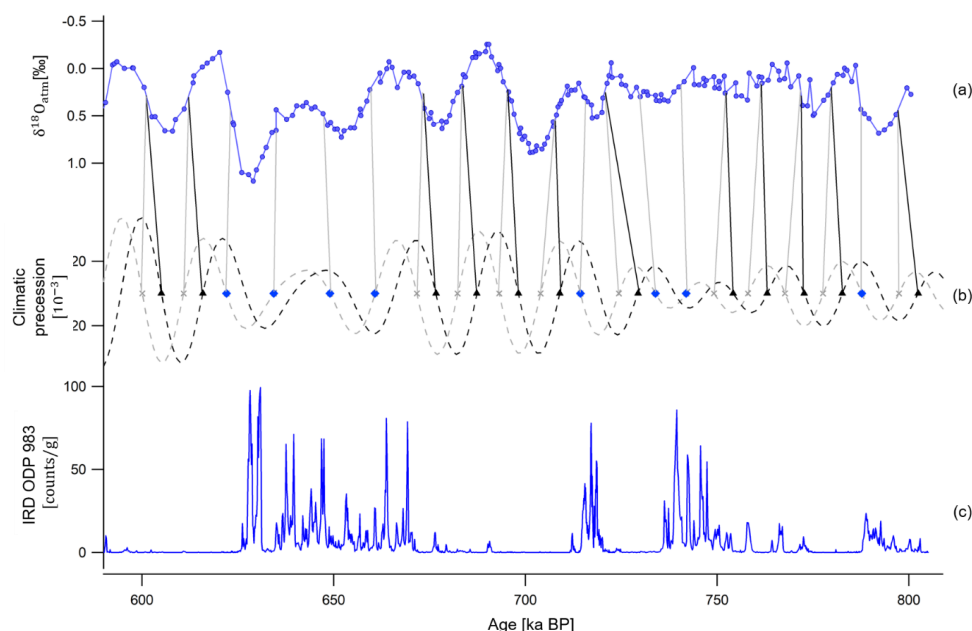
488 bars show tie points identified by Extier et al. (2018) that are not used in AICC2023. Red vertical areas frame periods of lacking  
489 resemblance between  $\delta^{18}\text{O}_{\text{atm}}$  and  $\delta^{18}\text{O}_{\text{calcite}}$  variations.

490

491 Between 810 and 590 ka BP, we updated the following approach of Bazin et al. (2013): EDC  $\delta^{18}\text{O}_{\text{atm}}$   
492 and 5 kyr delayed climatic precession are synchronized using mid-slopes of their variations. However,  $\delta^{18}\text{O}_{\text{atm}}$   
493 should rather be aligned to precession without delay when no Heinrich-like events occurs. Indeed,  $\delta^{18}\text{O}_{\text{atm}}$  is  
494 sensitive to both orbital and millennial scale variations of the low latitude water cycle (Capron et al., 2012a;  
495 Landais et al., 2010) and Heinrich-like events occurring during deglaciations delay the response of  $\delta^{18}\text{O}_{\text{atm}}$  to  
496 orbital forcing through southward ITCZ shifts (Extier et al., 2018). We thus chose to align  $\delta^{18}\text{O}_{\text{atm}}$  to precession  
497 when no Ice Rafted Debris (IRD) peak is visible on the studied period and keep a 5 kyr delay when IRD peaks are  
498 identified. This results in shifting 12 tie points of Bazin et al. (2013) by 5,000 years towards older ages (see Fig.  
499 6). The eight remaining tie points of Bazin et al. (2013) that coincide with peaks in the IRD record of Barker  
500 (2021) are kept (Fig. 6). A 6 kyr uncertainty is attributed to the  $\delta^{18}\text{O}_{\text{atm}}$  derived tie points over the period between  
501 810 and 590 ka BP.

502 69 new  $\delta^{18}\text{O}_{\text{atm}}$  tie points are determined here over the last 810 kyr (displayed in Fig. 5 and 6 and  
503 compiled in Table S1). They are attached to an uncertainty varying between 1.1 and 7.4 kyr and replace the 39 tie  
504 points used to constrain EDC gas timescale in AICC2012 between 800 and 363 ka BP (Bazin et al., 2013). The  
505 same alignment method is applied between Vostok  $\delta^{18}\text{O}_{\text{atm}}$  (Petit et al., 1999) and Chinese  $\delta^{18}\text{O}_{\text{calcite}}$  and 36 new  
506 tie points are determined (see Supplementary Material), replacing the 35 tie points used to constrain Vostok gas  
507 timescale in AICC2012.

508 Finally, there was a redundancy in the dating of the bottom part of the EDC ice core in AICC2012 where  
509 both  $\delta^{18}\text{O}_{\text{atm}}$  orbital tie points and  $^{10}\text{Be}$  peaks corresponding to the Matuyama - Brunhes geomagnetic reversal  
510 event were used. Indeed, the two  $^{10}\text{Be}$  dating constraints at 780.3 and 798.3 ka BP were directly derived from the  
511  $\delta^{18}\text{O}_{\text{atm}}$  orbital dating and not obtained independently (Dreyfus et al., 2008). We thus decided to remove the  $^{10}\text{Be}$   
512 age constraints.



513 **Figure 6. Alignment of EDC  $\delta^{18}\text{O}_{\text{atm}}$  and climatic precession between 810 and 590 ka BP.** (a) Compiled EDC  $\delta^{18}\text{O}_{\text{atm}}$   
 514 on AICC2012 gas timescale. (b) Precession delayed by 5,000 years (grey dashed line) and not delayed (black dashed line)  
 515 (Laskar et al., 2004). (c) Ice-Rafted Debris at ODP983 site (North Atlantic Ocean, southwest of Iceland) by Barker (2021).  
 516 Grey crosses represent mid-slopes of 5 kyr delayed precession variations. Grey vertical bars illustrate tie points between  
 517 precession and EDC  $\delta^{18}\text{O}_{\text{atm}}$  used by Bazin et al. (2013) to constrain AICC2012 gas timescale. Black triangles show mid-  
 518 slopes of variations of precession without delay. Black verticals bars display new tie points between precession and EDC  
 519  $\delta^{18}\text{O}_{\text{atm}}$  established when no Heinrich-like events is shown by IRD record. Blue squares represent mid-slopes of 5 kyr delayed  
 520 precession variations when Heinrich-like events are shown by IRD record. Black and blue markers correspond to the new tie  
 521 points defined in this study.

522

### 523 3.3 Background scenario of LID

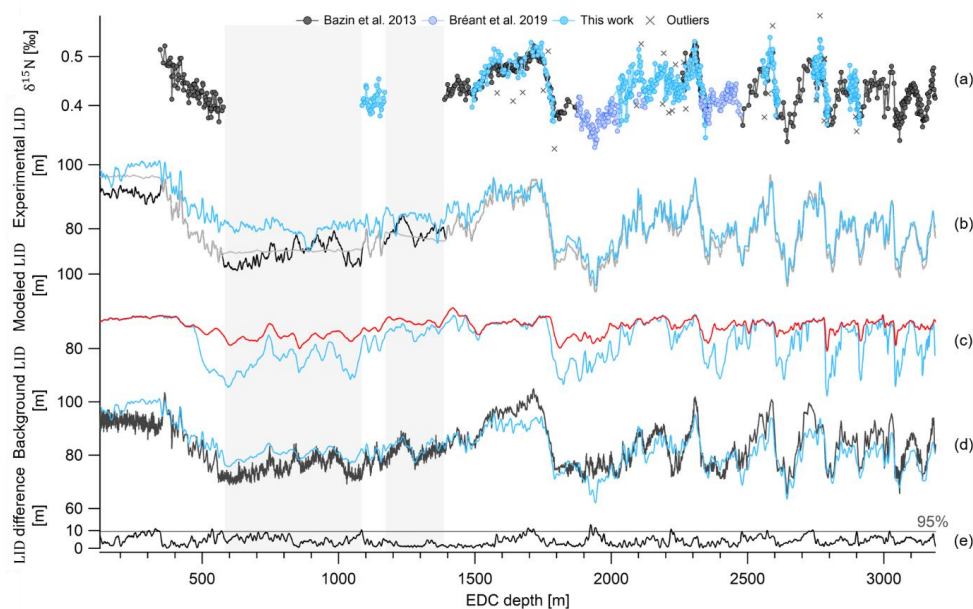
524 In this work, new highly resolved data  $\delta^{15}\text{N}$  on EDC ice core are presented over Terminations II, III, IV,  
 525 V and VI (Fig. 7a). The available  $\delta^{15}\text{N}$  data can be sorted out in two groups:  $\delta^{15}\text{N}$  measured by Grisart (2023) and  
 526 Bréant et al. (2019) at high temporal resolution (between 333 and 1,375 years, see Table 1) and the older  
 527 measurements (Bazin et al., 2013) used to estimate LID in AICC2012, characterised by a lower sampling resolution  
 528 (between 1,400 and 2,400 years, see Table 1). The measurements of Bazin et al. (2013) and Bréant et al. (2019)  
 529 have been shifted down by 0.04 ‰ to account for calibration errors. The new dataset permits to extend the record  
 530 around 1100 m and between 1700 and 2500 m and to improve the resolution over Terminations II to VI.

531

532

533

534



535 **Figure 7. EDC  $\delta^{15}\text{N}$  record and past LID evolution as a function of EDC depth.** (a) New and highly-resolved  $\delta^{15}\text{N}$  dataset  
 536 (blue circles), old dataset (black circles) and outliers (rejection criterion of  $1\sigma$ ) (grey crosses). (b) LID calculated as per  $LID \approx$   
 537  $\delta^{15}\text{N}_{\text{grav}} \cdot \frac{RT}{g}$  for 3 cases: 1)  $\delta^{15}\text{N}_{\text{grav}} = \delta^{15}\text{N}$  with the  $\delta^{15}\text{N}$  record constructed by interpolation between data when no data  
 538 are available (grey), 2)  $\delta^{15}\text{N}_{\text{grav}} = \delta^{15}\text{N}$  with the  $\delta^{15}\text{N}$  record constructed by normalisation of the  $\delta\text{D}$  record when no data are  
 539 available (black), 3)  $\delta^{15}\text{N}_{\text{grav}} = \delta^{15}\text{N} - \delta^{15}\text{N}_{\text{therm}}$  with  $\delta^{15}\text{N}_{\text{therm}}$  estimated by the firm model (Bréant et al., 2017) and the  
 540  $\delta^{15}\text{N}$  record constructed by interpolation between data when no data are available (blue). (c) Modeled LID according to test 1  
 541 (with impurity concentration, blue) and test 2 (without impurity concentration, red) (see Table 3). (d) Background scenarios of  
 542 LID used to construct AICC2012 (black) and inputs in PaleoChrono to obtain AICC2023 (blue). (e) Absolute difference  
 543 between prior LID of AICC2012 and AICC2023. The grey line separates the 5% highest values from the rest. The grey  
 544 rectangles cover areas when no  $\delta^{15}\text{N}$  data are available.

545 Outliers are discarded if they show an anomaly superior to 0.045 % when compared to the smoothed  
 546 record (Savitzky-Golay algorithm with 25 points). This results in the rejection of 25 datapoints out of 475  
 547 measurements for the new dataset (see Fig. 7). The two  $\delta^{15}\text{N}$  datasets are merged and the compiled record is  
 548 interpolated every 100 years. Then, assuming that the firm is solely a diffusive zone (i.e. no convection layer at the  
 549 top) at EDC during the last 800 kyr, in agreement with current observations (Landais et al., 2006), past LID is  
 550 calculated as per the first order estimate of the barometric equation:

$$551 \quad LID \approx \delta^{15}\text{N}_{\text{grav}} \cdot \frac{RT}{g} \quad (5)$$

552 with  $T$  the temperature at EDC estimated from combined measurements of ice  $\delta^{18}\text{O}$  and  $\delta\text{D}$  after correction of  
 553 the influence of the sea water  $\delta^{18}\text{O}$  (Landais et al., 2021).

554 In absence of a large thermal gradient within the firm (mostly present in Greenlandic ice cores during  
 555 Dansgaard Oeschger events),  $\delta^{15}\text{N}$  is mainly modulated by gravitational fractionation of  $\text{N}_2$  molecules occurring  
 556 from the surface down to the lock-in zone, and  $\delta^{15}\text{N}$  measured in bubbles hence approximately reflects the LID



557 (Landais et al., 2006; Severinghaus et al., 1996) and  $\delta^{15}\text{N}_{\text{grav}} \approx \delta^{15}\text{N}$  in Eq. (5) (grey and black lines in Fig. 7b).  
 558 To account for a small temperature gradient in the firn in Antarctic ice core, the thermal fractionation term  
 559  $\delta^{15}\text{N}_{\text{therm}}$  can be estimated by the firn model (Bréant et al., 2017). Past LID is then calculated as per Eq. (5) with  
 560  $\delta^{15}\text{N}_{\text{grav}} = \delta^{15}\text{N} - \delta^{15}\text{N}_{\text{therm}}$  (blue curve in Fig. 7b). Thermal fractionation represents a maximum correction of  
 561 4.2 m on the LID at EDC.

562 When  $\delta^{15}\text{N}$  measurements are not available, Bazin et al. (2013) used a synthetic  $\delta^{15}\text{N}$  signal based on the  
 563 correlation between  $\delta^{15}\text{N}$  and  $\delta\text{D}$  to estimate the LID background scenario (black curve in Fig. 7b). Indeed, for  
 564 different Antarctic sites, it has been observed that  $\delta^{15}\text{N}$  and  $\delta\text{D}$  are well correlated over the last Termination on a  
 565 coherent timescale (Dreyfus et al., 2010; Capron et al., 2013). Since then, Bréant et al. (2019) presented new high  
 566 resolution measurements of  $\delta^{15}\text{N}$  extending the signal over Termination III (around 2300 m, 250 ka BP). Their  
 567 study unveiled the anatomy of this atypical deglaciation: the interplay between Heinrich-like events and bipolar  
 568 seesaw mechanism induced a strong warming of Antarctic temperature, resulting in divergent  $\delta^{15}\text{N}$  and  $\delta\text{D}$   
 569 records. Therefore, using  $\delta\text{D}$  to construct a synthetic  $\delta^{15}\text{N}$  scenario should be done carefully. For this reason, the  
 570 firn densification model described in Bréant et al. (2017) is employed to estimate LID evolution in the past when  
 571  $\delta^{15}\text{N}$  data are missing, rather than using the  $\delta\text{D} - \delta^{15}\text{N}$  relationship, as it was done for AICC2012. After different  
 572 sensitivity tests, we choose to keep the parameterization preferred by Bréant et al. (2017): test 1 in Table 3 (i.e.  
 573 firn densification activation energy depending on the temperature and the impurity concentration) as it is believed  
 574 to give the most probable evolution of LID over the last 800 kyr (see Supplementary Material).

575 The final LID background scenario is calculated as a function of EDC depth (Table 5, Fig. 7d). To obtain  
 576 a coherent scenario, the firn modeling estimates have been adjusted, by standard normalization, to the scale of LID  
 577 values derived from  $\delta^{15}\text{N}$  data (later referred to as experimental LID). The final LID scenario has been smoothed  
 578 using a Savitzky-Golay algorithm (25 points), and then provided as an input file to Paleochrono.

579

580 **Table 5. Method of determination of LID background scenario according to EDC depth range.** The thermal fractionation  
 581 term is estimated by the firn model running in the same configuration as for calculating the modeled LID, i.e. Test 1 (Table 3):  
 582 Firn densification activation energy depending on the temperature and impurity concentration.

Depth range (m)	0 – 345	345 - 578	578 - 1086	1086 – 1169	1169 – 1386	1386 – Bottom
<b><math>\delta^{15}\text{N}</math> data availability</b>	No	Yes	No	Yes	No	Yes
<b>Method of determination of the LID</b>	From constant $\delta^{15}\text{N}$ (measured at 345 m) and corrected for thermal fractionation.	From $\delta^{15}\text{N}$ data, corrected for thermal fractionation and smoothed.	From firn modeling and scaled to experimental LID values.	From $\delta^{15}\text{N}$ data, corrected for thermal fractionation and smoothed.	From firn modeling and scaled to experimental LID values.	From $\delta^{15}\text{N}$ data, corrected for thermal fractionation and smoothed.

583



584 The other necessary input files for Paleochrono, Accumulation ( $A$ ) and Thinning ( $\tau$ ) background scenarios,  
585 are the same as in Bazin et al. (2013).  $A$  is estimated from water isotopes (Parrenin et al., 2007b) and  $\tau$  from  
586 unidimensional ice-flow modeling (Parrenin et al., 2007a).

### 587 **3.4 New stratigraphic links between EDC and other ice cores**

588 EDC can be linked to other ice cores via ice and gas stratigraphic links identified during abrupt climate  
589 changes recorded in Greenlandic and Antarctic ice cores. To establish AICC2012, Bazin et al. (2013) used 255  
590 gas stratigraphic tie points coming from the matching of  $\text{CH}_4$  (or  $\delta^{15}\text{N}$  when  $\text{CH}_4$  is not available at NGRIP) or  
591  $\delta^{18}\text{O}_{\text{atm}}$  variations between EDC, EDML, Vostok, NGRIP and TALDICE. Here we revise the majority of these  
592 tie points using the synchronization of  $\text{CH}_4$  series of EDC, Vostok and TALDICE to up-to-date highly resolved  
593 records from EDML and NGRIP ice cores over the last interglacial offset and the last glacial period (Baumgartner  
594 et al., 2014). From 122 to 10 ka BP, Baumgartner et al. (2014) identified 39 stratigraphic links between EDML  
595 and NGRIP by matching mid-points of the  $\text{CH}_4$  abrupt changes with a precision of 300 to 700 years. When they  
596 also detected such rapid variations in lower resolved  $\text{CH}_4$  records of TALDICE, Vostok and EDC ice cores, they  
597 extended the stratigraphic links to the five ice cores but assigned them a larger uncertainty (up to 1,500 years).  
598 AICC2012 was further constrained by 534 ice stratigraphic links identified from volcanic matching and  
599 synchronization of cosmogenic isotopes between the five ice cores. Here we replace some of the stratigraphic links  
600 between NGRIP, EDML and EDC by highly resolved volcanic matching points (Svensson et al., 2020). The  
601 application of volcanic proxies and annual layer counting helped them identify large volcanic eruptions that left a  
602 specific signature in both Greenland and Antarctica. Such signature is defined by sulfate patterns (indicating  
603 singular volcanic events separated by the same time interval in ice cores from both poles). Their study spotted 82  
604 large bipolar volcanic eruptions over the second half of the last glacial period (from 60 to 12 ka BP), providing as  
605 many ice stratigraphic links synchronising EDC with EDML and EDML with NGRIP within a small relative  
606 uncertainty (i.e. ranging from 1 to 50 years, of 12 years on average). Between 43 and 40 ka BP, five cosmogenic  
607 tie points associated with the Laschamp geomagnetic excursion (Raisbeck et al., 2017) replace the volcanic  
608 matching over this period (Svensson et al., 2013), shifting the tie points by  $\sim 30$  years.

## 609 **4 Discussion**

### 610 **4.1 New AICC2023 chronology**

#### 611 **4.1.1 Impact of absolute age constraints**

612 A large uncertainty is linked with  $^{81}\text{Kr}$  dating, therefore  $^{81}\text{Kr}$  age estimates do not significantly change  
613 the chronology (maximum 200 years) (see Fig. 8).  $^{81}\text{Kr}$  age estimates are systematically older than the new  
614 timescale (by 25 to 36 kyr, see Fig. 9). This observation could also indicate an undervaluation of  $^{81}\text{Kr}$  half-life.

#### 615 **4.1.2 Consistency between orbital age constraints**

616 To evaluate the consistency between the orbital age constraints, several “test chronologies” were  
617 produced. Each “test chronology” of EDC ice core was obtained by running one multi-site (EDC, Vostok, EDML,  
618 TALDICE, NGRIP) experiment of Paleochrono. In each of these tests, we implement one category of new age  
619 constraints presented in this work while keeping AICC2012 parameters for other categories. Several “test  
620 chronologies” are thus constructed: the  $^{81}\text{Kr}$ ,  $\delta\text{O}_2/\text{N}_2$ , TAC,  $\delta^{18}\text{O}_{\text{atm}}$  and stratigraphic links based chronologies



621 (Fig. 8). Two additional “test chronologies” were obtained by implementing and modifying age constraints either  
622 on Vostok or TALDICE to the AICC2012 chronology as explained in Sect. 2.a (Fig. 8, dotted lines). EDC ice age  
623 difference between each “test chronology” and the AICC2012 timescale is represented in Fig. 8 so that it is possible  
624 to read which type of dating tool suggests to shift the background chronology towards either older or younger ages.

625 Although the three orbital dating tools globally agree with each other over the last 800 kyr, meaning that  
626 they all tend to shift the background chronology towards either older or younger ages over a certain period of time,  
627 they sometimes are inconsistent (see Fig. 8). The three largest inconsistencies involve age differences between  
628  $\delta O_2/N_2$ , TAC and  $\delta^{18}O_{atm}$  based chronologies reaching 4.15 to 8.3 kyr (Table 6). At 390 ka BP, an 8.3 kyr large  
629 discrepancy is observed between  $\delta O_2/N_2$  and  $\delta^{18}O_{atm}$  based chronologies. Over this period, the low resolution  
630  $\delta O_2/N_2$  record variations do not match its orbital target variations (two insolation minima against one  $\delta O_2/N_2$   
631 maximum, see Fig. 1). For this reason, the  $\delta O_2/N_2$  age constraints identified between 480 and 350 ka BP were  
632 attached to a 6 kyr uncertainty (quarter of a recession period, Fig. 2). In contrast, the  $\delta^{18}O_{atm}$  record agrees well  
633 with  $\delta^{18}O_{calcite}$  (Fig. 4) and the uncertainty attached to the  $\delta^{18}O_{atm}$  inferred tie points over this interval is smaller.  
634 Hence, the new AICC2023 chronology suggests to shift AICC2012 towards older ages by 2.2 kyr, as per the  
635  $\delta^{18}O_{atm}$  based chronology (Fig. 8). Around 550 ka BP, the TAC and  $\delta^{18}O_{atm}$  based chronologies strongly diverge.  
636 This may be caused by the absence of TAC tie points due to the non-coincidence of TAC and ISI375 extrema (Fig.  
637 3) while there is a good agreement between  $\delta^{18}O_{atm}$  and  $\delta^{18}O_{calcite}$  records. Therefore, we decide to increase up  
638 to 6 kyr the uncertainty attached to the four TAC age constraints between 600 and 550 ka BP (Fig. 3) and  
639 AICC2023 is rather following the  $\delta^{18}O_{atm}$  based chronology, inducing older ages than AICC2012. At 765 ka BP,  
640 the discordance between  $\delta O_2/N_2$  (and TAC) and  $\delta^{18}O_{atm}$  based chronologies is likely due to the poor quality of  
641 the records from the lowermost part of the core. Over these oldest time periods,  $\delta^{18}O_{atm}$ , TAC and  $\delta O_2/N_2$  were  
642 tied up respectively with precession, integrated insolation and insolation with a large uncertainty (6 to 10 kyr).  
643 This leads to a final chronology AICC2023 suggesting a larger chronological uncertainty than AICC2012 as well  
644 as younger ages (as per TAC and  $\delta O_2/N_2$  chronologies) over MIS 18, and then older ages (as per  $\delta^{18}O_{atm}$   
645 chronology) over MIS 19.

646

647

648

649

650

651

652

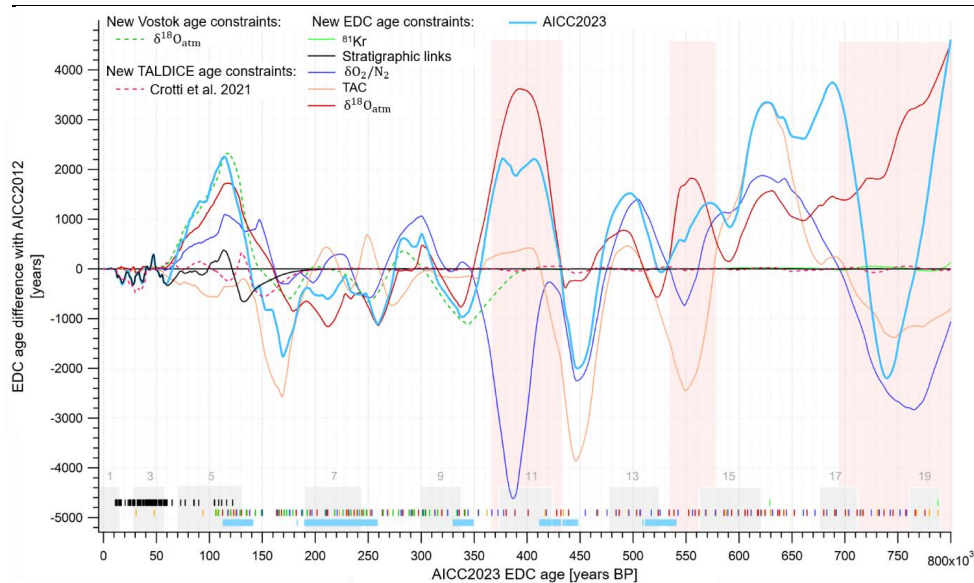
653

654



655 **Table 6. Description of the inconsistencies between TAC,  $\delta O_2/N_2$  and  $\delta^{18}O_{atm}$  based chronologies.** The age shift  
 656 suggested by each dating tool with respect to AICC2012 age is detailed. The age position of the disagreement is given as per  
 657 AICC2023. We did not highlight inconsistencies between TAC and  $\delta O_2/N_2$  based chronologies as they remain within their  
 658 respective orbital uncertainty.

		$\delta^{18}O_{atm}$		
$\delta O_2/N_2$	Non-coherent	Non-coherent	Non-coherent	
TAC	Coherent	Non-coherent	Non-coherent	
<b>Disagreement type</b>	$\delta O_2/N_2$ chronology younger by 4,700 years than AICC2012	TAC (and $\delta O_2/N_2$ ) chronology younger by 2,400 (and 800) years than AICC2012	$\delta O_2/N_2$ (and TAC) chronology younger by 2,850 (and 1,300) years than AICC2012	
	$\delta^{18}O_{atm}$ chronology older by 3,600 years than AICC2012	$\delta^{18}O_{atm}$ chronology older by 1,700 years than AICC2012	$\delta^{18}O_{atm}$ chronology older by 2,800 years than AICC2012	
<b>Interval of disagreement (ka BP)</b>	390 (MIS 11)	550 (MIS 14)	765 (MIS 19)	



659 **Figure 8. EDC ice age difference between AICC2012 and different tests chronologies obtained with Paleochrono over**  
 660 **the last 800 kyr.** The ice age difference is calculated as per (“test chronology” – AICC2012). Two “test chronologies” are  
 661 obtained either by addition of new Vostok  $\delta^{18}O_{atm} - \delta^{18}O_{calcite}$  age constraints (green dotted line) or of stratigraphic and  
 662 absolute TALDICE constraints between 470 and 129 ka BP from Crotti et al. (2021) (red dotted line). The other “test  
 663 chronologies” are constructed by implementing either: 1)  $^{81}Kr$  (green), 2)  $\delta O_2/N_2$  (dark blue), 3) TAC (orange), 4)  $\delta^{18}O_{atm}$   
 664 (red) and 5) stratigraphic links with NGRIP, EDML, TALDICE, Vostok (black) to replace AICC2012 constraints. Vertical bars  
 665 represent the corresponding age horizons. AICC2023 is obtained by implementing the new constraints all together (light blue

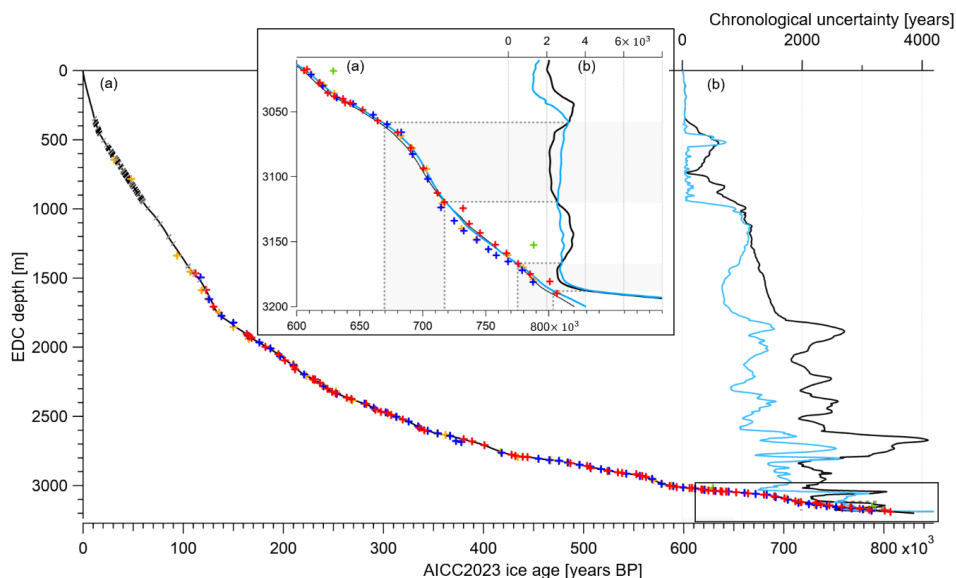




666 line). Light blue vertical bars show new data collected by Grisart (2023) and presented in this work. The three largest  
 667 inconsistencies between  $\delta\text{O}_2/\text{N}_2$ , TAC and  $\delta^{18}\text{O}_{\text{atm}}$  chronologies are shown by red areas. Grey squares indicate interglacials  
 668 from MIS 19 to MIS 1.

### 669 4.1.3 Final chronology and uncertainty

670 The new AICC2023 chronology suggests significant age shifts when compared to AICC2012 over old  
 671 periods, including 3.8 and 5 kyr shifts towards older ages around 800 and 690 ka BP as well as a 2.1 kyr shift  
 672 towards younger ages around 730 ka BP. The chronology is also strongly modified over MIS 5 and MIS 11 where  
 673 AICC2023 is about 2 kyr older than AICC2012. These 2 kyr shifts are induced by  $\delta\text{O}_2/\text{N}_2$ ,  $\delta^{18}\text{O}_{\text{atm}}$  dating  
 674 constraints and stratigraphic links over MIS 5 and by  $\delta^{18}\text{O}_{\text{atm}}$  and TAC constraints over MIS 11. When averaged  
 675 over the past 800 kyr, the chronological uncertainty is reduced from 2.5 kyr for AICC2012 to 1.8 kyr here. Still, it  
 676 remains significant (above 2 kyr) over MIS 11 and in the lowermost part of the core, between 800 and 650 ka BP.  
 677 Specifically, between 800 and 670 ka BP, the uncertainty associated with the new AICC2023 timescale sometimes  
 678 is larger than the AICC2012 uncertainty (Fig. 9). This is caused by a larger relative error attached to TAC and  
 679  $\delta\text{O}_2/\text{N}_2$  age constraints as well as by the eviction of the two redundant  $^{10}\text{Be}$  age constraints at 780.3 and 798.3 ka  
 680 BP associated with the Matuyama - Brunhes geomagnetic reversal event.

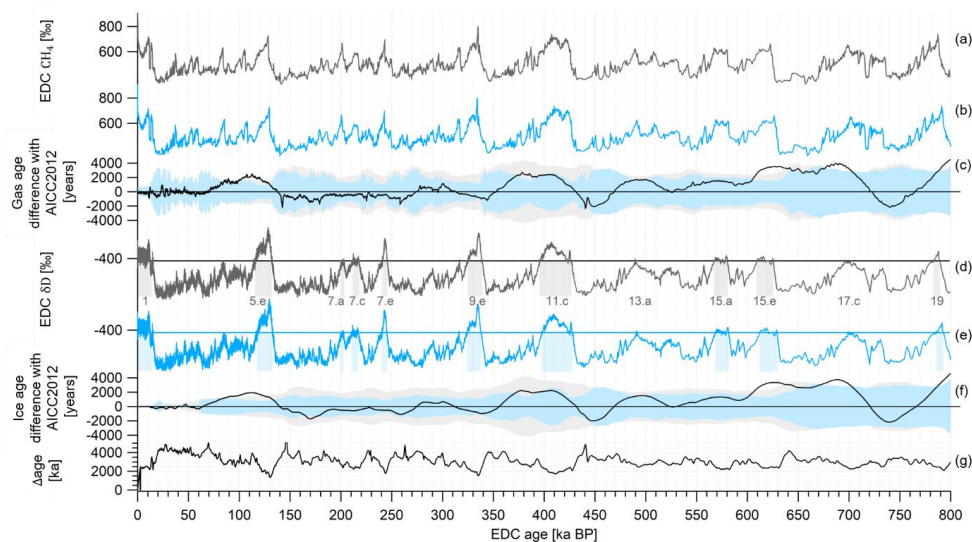


681 **Figure 9. EDC ice age and uncertainty as a function of the depth.** (a) EDC ice age (AICC2012 in black, AICC2023 in blue).  
 682 (b) Uncertainty (AICC2012 in black, AICC2023 in blue). Crosses and slashes represent new age constraints (ice stratigraphic  
 683 links in black, gas stratigraphic links in grey,  $\delta^{18}\text{O}_{\text{atm}}$  in red,  $\delta\text{O}_2/\text{N}_2$  in blue, TAC in orange,  $^{81}\text{Kr}$  in green). Inset is a zoom  
 684 in between 800 and 600 ka BP. Grey rectangles frame periods where the new AICC2023 uncertainty is larger than AICC2012  
 685 uncertainty.

686 The age difference between ice and gas timescales ( $\Delta\text{age}$ ) is of 3 kyr on average, reaching its largest value  
 687 (5 kyr) during the colderas of MIS 12, 8, 6 and 4 (at 440, 260, 145 and 70 ka BP respectively, Fig. 10). A 4 kyr  
 688  $\Delta\text{age}$  is obtained at around 160 ka BP (Fig. 10), consistent with the use of new  $\delta^{15}\text{N}$  data of Bréant et al. (2019)



689 leading to a background scenario of LID that is 13 m smaller than the prior LID scenario used in AICC2012  
 690 between the depths of 1900 and 2000 m (Fig. 7). Using the definition of an interglacial period implying an EDC  
 691  $\delta D$  value surpassing the threshold of - 403 ‰ (EPICA Community members, 2004), we identify ten substages of  
 692 interglacials (MIS 1, 5e, 7a, 7c, 7e, 9e, 11c, 15a, 15e and 19, Fig. 10). The average duration of these substages is  
 693 reduced by 320 years with the new AICC2023 timescale in comparison with the AICC2012 chronology (Fig. 10).  
 694 More specifically, MIS 5e to 15a are shorter while only MIS 15e and MIS 19 are longer. The largest decreases in  
 695 duration affecting the Last Interglacial (MIS 5e) and MIS 11.c whose lengths are decreased from 16.3 to 15.1 kyr  
 696 and from 31.1 to 30.1 kyr respectively, in agreement with the durations of 14.8 and 29.7 kyr proposed by Extier et  
 697 al. (2018).



698 **Figure 10. EDC gas and ice records on AICC2023 (blue) and AICC2012 (black) timescales over the last 800 kyr.** (a)  
 699 EDC  $CH_4$  on AICC2012 and (b) AICC2023 gas timescales. (c) Gas age difference AICC2023 – AICC2012. Grey and blue  
 700 envelopes are AICC2012 and AICC2023 chronological uncertainties respectively. (d) EDC  $\delta D$  on AICC2012 and (e) AICC2023  
 701 ice timescales. Grey and blue rectangles indicate interglacial periods defined when  $\delta D$  is superior to the threshold of - 403 ‰  
 702 (horizontal lines) (EPICA members, 2004). Interglacials are numbered from MIS 1 to 19 (Berger et al., 2016). (f) Ice age  
 703 difference AICC2023 – AICC2012. (g) Age difference between ice and gas AICC2023 timescales ( $\Delta age$ ).

704

## 705 4.2 Comparison with other chronologies

### 706 4.2.1 MIS 5 (from 130 to 80 ka BP)

707 When Veres et al. (2013) presented the AICC2012 chronology over the last climatic cycle, they identified  
 708 a disagreement with the Greenland timescale GICC05-modelext between 115 and 100 ka BP. The comparison  
 709 between the Greenland  $\delta^{18}O_{ice}$  record and the  $\delta^{18}O_{calcite}$  from U-Th dated Alpine speleothems shown a delay up  
 710 to 2.7 kyr during the Dansgaard Oeschger (D-O) events 23, 24 and 25. Later, this disagreement between abrupt  
 711 changes in  $\delta^{18}O_{ice}$  from NGRIP (Greenland surface temperature) and  $\delta^{18}O_{calcite}$  from the Alps has been re-



712 evaluated based on a new ice core chronology. Extier et al. (2018) presented a better agreement between the two  
 713 records with an older NGRIP timescale than AICC2012 by ~2,200 years for D-O 23 to 25.

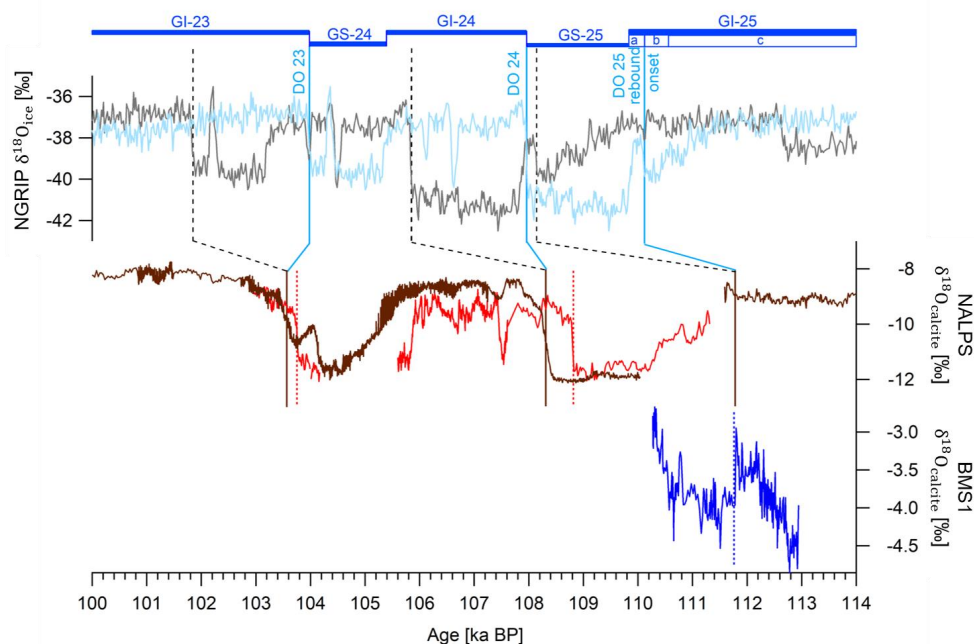
714 On Fig. 11, NGRIP  $\delta^{18}\text{O}_{\text{ice}}$  record is represented on the AICC2023 timescale and is compared to ancient and novel  
 715 records of  $\delta^{18}\text{O}_{\text{calcite}}$  from Alpine speleothems (Bochet et al., 2011; Moseley et al., 2020). Thanks to new  $\delta\text{O}_2/\text{N}_2$   
 716 and  $\delta^{18}\text{O}_{\text{atm}}$  age constraints, the new AICC2023 chronology is also older than AICC2012 between 115 and 100  
 717 ka BP and leads to an improved agreement between the records along with a reduction of the uncertainty. This  
 718 amelioration is particularly visible over D-O warmings 23 and 24 where the difference between NALPS and  
 719 NGRIP chronologies is reduced from ~2,000 years (AICC2012) to 430 and 325 years (AICC2023) respectively  
 720 (Table 7).

721 The Greenland Interstadial (GI) 25 can be subdivided in three substages: GI-25a-b-c with GI-25a the  
 722 earliest glacial so-called “rebound event” (Capron et al., 2010). This latter consists in a brief warm-wet excursion  
 723 during the slow cooling trend of the longer GI-25 period, before jumping back to a cool-dry climate. The GI-25a  
 724 warm-wet interval corresponds to a temperature increase in Greenland and continental Europe and hence identified  
 725 by a positive excursion in NGRIP and NALPS  $\delta^{18}\text{O}$  records (D-O 25 rebound) (Bochet et al., 2011; Capron et al.,  
 726 2012). At lower latitudes, this rebound likely affected the rainfall amount variations, as exhibited by the abrupt  
 727 decrease in the  $\delta^{18}\text{O}_{\text{calcite}}$  from a U-Th dated Sardinian stalagmite from Bue Marino Cave (BMS1, Columbu et  
 728 al., 2017). The 2 kyr shift of the new AICC2023 chronology towards older ages permits to improve the coherency  
 729 between NALPS, NGRIP and BMS1 timescales over the GI-25a onset (traceable in the  $\delta^{18}\text{O}$  series, Fig. 11). The  
 730 age discrepancy is reduced from ~3,600 years (between AICC2012 and BMS1 timescale) to 1,640 years (between  
 731 AICC2023 and BMS1 timescale, Table 7).

732 **Table 7. Timing of D-O warmings 23 and 24 and D-O 25 rebound event onset.** The GICC05-modelext age uncertainty is  
 733 undetermined.

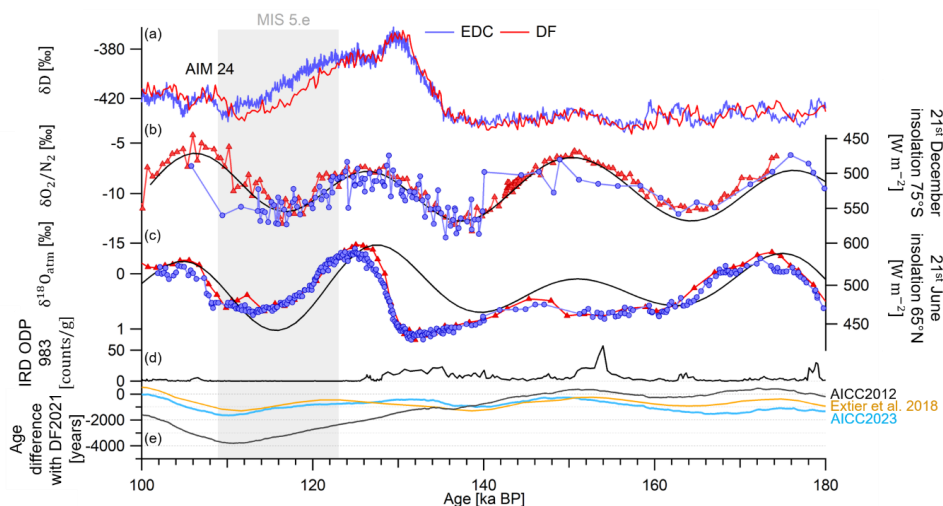
Event	Timing (a BP) and error (years)					
	NGRIP ice core timescale				Speleothem timescale	
	GICC05- modelext (Wolff et al., 2010)	AICC2012 (Veres et al. 2013)	Extier et al. (2018)	AICC2023 (This study)	BMS1 (Columbu et al. 2017)	NALPS (Bochet et al. 2021)
D-O 23 warming	103 995	101 850 ± 1310	104 090 ± 1200	103 980 ± 930	Not recorded	103 550 ± 375
D-O 24 warming	108 250	105 850 ± 1330	108 010 ± 1200	107 975 ± 850	Not recorded	108 300 ± 450
D-O 25 rebound onset	110 960	108 100 ± 1410	110 280 ± 1200	110 120 ± 900	111 760 ± 450	111 780 ± 630

734



735 **Figure 11. Northern Alpine speleothems (NALPS) and Bue Marino Stalagmite (BMS1)  $\delta^{18}\text{O}_{\text{calcite}}$  records and NGRIP**  
 736  **$\delta^{18}\text{O}_{\text{ice}}$  evolution between 114 and 100 ka BP.** NGRIP  $\delta^{18}\text{O}_{\text{ice}}$  data by Andersen et al. (2004) on AICC2012 (grey) and  
 737 AICC2023 (blue) chronologies. NALPS  $\delta^{18}\text{O}_{\text{calcite}}$  data by Moseley et al. (2020) (red) and Boch et al. (2011) (brown). BMS1  
 738  $\delta^{18}\text{O}_{\text{calcite}}$  data by Colombu et al. (2017) (dark blue). Vertical bars indicate D-O 23, D-O 24 and D-O 25 rebound warmings  
 739 at the onset of GI-23, GI-24 and GI-25a warm-wet substage. They correspond to abrupt increases in the NALPS  $\delta^{18}\text{O}_{\text{calcite}}$  and  
 740 NGRIP  $\delta^{18}\text{O}_{\text{ice}}$  records and to a decrease in the BMS1  $\delta^{18}\text{O}_{\text{calcite}}$  series (for the GI-25a onset). Black dashed bars and blue  
 741 bars show increases in  $\delta^{18}\text{O}_{\text{ice}}$ , respectively on AICC2012 and AICC2023 chronologies. Brown bars and red dotted bars show  
 742 increases in NALPS  $\delta^{18}\text{O}_{\text{calcite}}$  datasets. The blue dotted bar indicates the decrease in BMS1  $\delta^{18}\text{O}_{\text{calcite}}$ . GI/GS (Greenland  
 743 Stadials) boundaries and GI-25 subdivision are indicated on the new AICC2023 chronology by horizontal bars.

744 Between 128 and 103 ka BP, the comparison between the AICC2012 timescale and the novel Dome Fuji  
 745 ice core DF2021 chronology indicates that AICC2012 is likely too young by up to 4 kyr. Here, thanks to new  
 746 highly resolved  $\delta\text{O}_2/\text{N}_2$  data and to the alignment of  $\delta^{18}\text{O}_{\text{atm}}$  and  $\delta^{18}\text{O}_{\text{calcite}}$  records, we improve the consistency  
 747 between AICC2023 and DF2021, now agreeing within 1.7 kyr over MIS 5e (Fig. 12). With the new chronologies,  
 748 the records of  $\delta^{18}\text{O}_{\text{atm}}$  and  $\delta\text{O}_2/\text{N}_2$  from Dome Fuji and EDC ice cores show synchronous variations between 140  
 749 and 115 ka BP although the  $\delta\text{O}_2/\text{N}_2$  measurements from EDC are more scattered than DF data due to the use of  
 750 smaller samples (see Supplementary material). However,  $\delta\text{D}$  records still are slightly discordant and EDC record  
 751 lags DF by up to 1,700 years over MIS 5.e and at the onset of the Antarctic Isotope Maximum (AIM) 24 (Fig. 12),  
 752 suggesting some remaining chronology problems (AIM 24 onset) or regional climatic differences ( $\delta\text{D}$  decrease  
 753 over MIS 5.e). Between 180 and 150 ka BP, AICC2012 shows a better agreement with the DF2021 chronology  
 754 than the new AICC2023 chronology which suggests younger ages as per TAC and  $\delta^{18}\text{O}_{\text{atm}}$  dating constraints.



755 **Figure 12. Evolution of EDC and DF records on AICC2023 and DF2021 chronologies between 180 and 100 ka BP.** (a)  
 756  $\delta D$  records from DF (red, Uemura et al., 2018) and EDC (blue, Jouzel et al., 2007). (b)  $\delta O_2/N_2$  records from DF (red triangles,  
 757 Oyabu et al., 2022) and EDC (blue circles, this work). (c)  $\delta^{18}O_{atm}$  records from DF (red triangles, Kawamura et al., 2007) and  
 758 EDC (blue circles, this work). DF and EDC records are represented on DF2021 and AICC2023 timescales. (d) IRD from ODP  
 759 983 (Barker et al., 2021). (e) Ice age difference between DF2021 and AICC2023 (blue), Extier et al. (2018) chronology (orange)  
 760 and AICC2012 (black). The age difference is calculated as per EDC age – DF2021 age. DF2021 age is transferred onto EDC  
 761 ice core via the volcanic synchronisation of Fujita et al. (2015). Grey rectangle indicates MIS 5e.

762

#### 763 4.2.2 MIS 11 (from 405 to 380 ka BP)

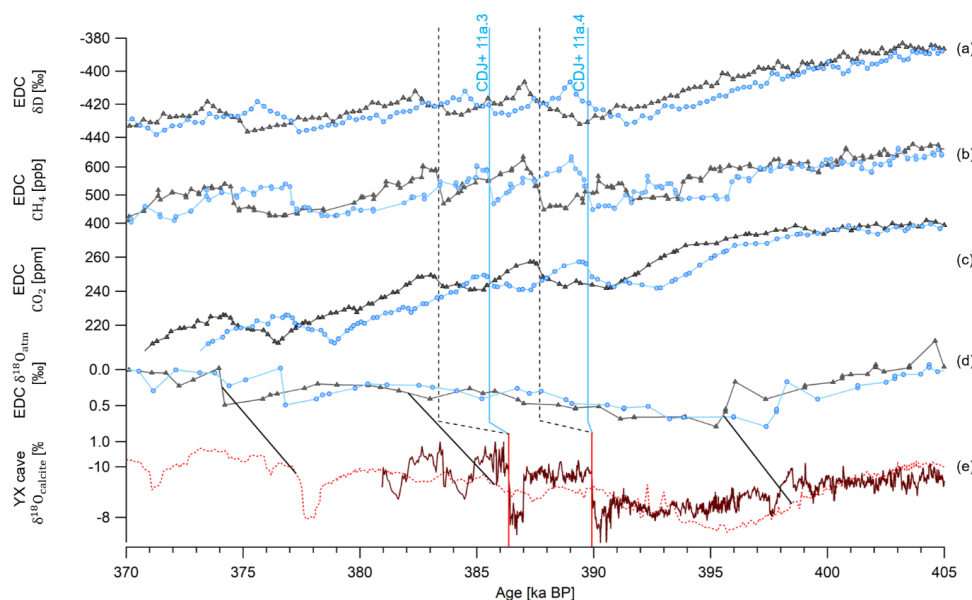
764 Over the MIS 11 (from ~398 to 370 ka BP), the new AICC2023 chronology predicts older ages than  
 765 AICC2012 (by up to 2 kyr) with a diminished uncertainty (from 3.9 to 1.6 kyr). This shift towards older ages is  
 766 induced by  $\delta^{18}O_{atm} - \delta^{18}O_{calcite}$  (Hulu, Sambao and Dongge caves) tie points at 377.3, 385.8 and 395.6 ka BP and  
 767 by the TAC age constraint at 362.1 ka BP (Fig. 8, 13). As a result, two major rises in the EDC atmospheric  $CO_2$   
 768 and  $CH_4$  concentration records (corresponding to Carbon Dioxide Jumps, CDJ+ 11a.3 and 11a.4, labelled as per  
 769 Nehrbass-Ahles et al., 2020) occur at  $385.6 \pm 1.4$  and  $389.8 \pm 1.5$  ka BP (Fig. 13). These two rapid jumps in  $CO_2$   
 770 and  $CH_4$  are better aligned with two abrupt decreases in the highly resolved  $\delta^{18}O_{calcite}$  record of Zhao et al. (2019)  
 771 from Yongxing cave (dated at  $386.4 \pm 3.1$  and  $390.0 \pm 3.0$  ka BP) than when using the AICC2012 chronology  
 772 (improvement by ~800 years). Such millennial-scale synchronicity is expected between  $CH_4$  and  $\delta^{18}O_{calcite}$  series  
 773 from Chinese speleothems as they both are influenced by Asian monsoon area displacements (and associated  
 774 methane emissions from wetlands) (Sánchez Goñi et al., 2008).

775

776

777

778



779 **Figure 13. Evolution of climate tracers from EDC ice core and Yongxing cave stalagmites between 405 and 380 ka BP.**  
 780 EDC records of (a)  $\delta D$ , (b)  $CH_4$  (Nehrbass-Ahles et al., 2020), (c)  $CO_2$  (Nehrbass-Ahles et al., 2020) and (d)  $\delta^{18}O_{atm}$  on  
 781 AICC2012 (grey triangles) and AICC2023 (blue circles) chronologies. (e)  $\delta^{18}O_{calcite}$  from U-Th dated speleothems from Hulu,  
 782 Dongge and Sambaocave (dashed red curve) and Yongxing (YX) cave (brown plain curve) (Zhao et al., 2019). CDJ+ are  
 783 labelled as per Nehrbass-Ahles et al. (2020). Dashed black and blue vertical bars show jumps in  $CO_2$  respectively on AICC2012  
 784 and AICC2023 chronologies, red vertical bars show corresponding decreases in  $\delta^{18}O_{calcite}$ . Black lines show the three tie  
 785 points between  $\delta^{18}O_{atm}$  and SB cave  $\delta^{18}O_{calcite}$  used to constrain AICC2023.

786

#### 787 4.2.3 MIS 19 (from 780 to 760 ka BP)

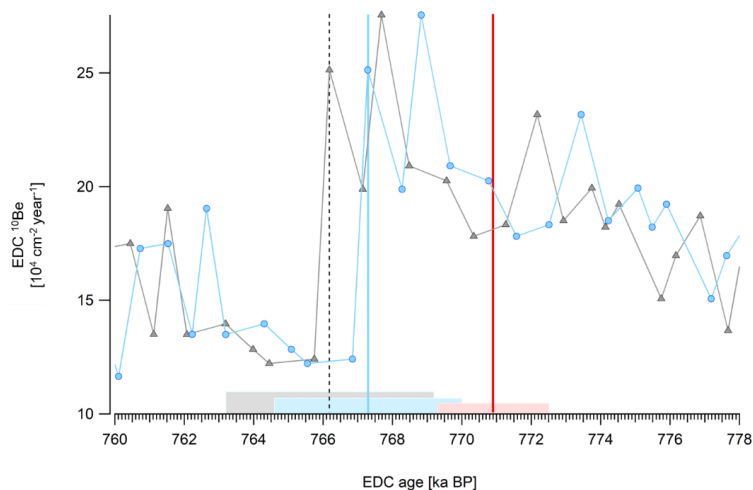
788 The Matuyama-Brunhes (MB) event (geomagnetic field reversal) is reflected by a globally synchronous  
 789 event in the  $^{10}Be$  signal: an abrupt termination of the large  $^{10}Be$  peak following a long-term increasing trend  
 790 recorded in both ice and sedimentary cores (Giaccio et al., 2023). The  $^{40}Ar/^{39}Ar$  age constrained chronology of a  
 791 lacustrine succession from Sulmona basin (Giaccio et al., 2023) gives an age of  $770.9 \pm 1.6$  ka BP for the  $^{10}Be$   
 792 peak termination. The new AICC2023 chronology provides an estimate of  $767.3 \pm 3$  ka BP for the same  $^{10}Be$  peak  
 793 termination, an age which is closer to the  $^{40}Ar/^{39}Ar$  age evaluation than the AICC2012 chronology estimate  
 794 ( $766.2 \pm 3$  ka BP, Fig. 14). The new AICC2023 chronology indeed indicates an increasing older age than  
 795 AICC2012 over MIS 19 (from 790 to 761 ka BP) due to the new  $\delta^{18}O_{atm}$  based timescale (Fig. 8).

796

797

798

799



800 **Figure 14. EDC  $^{10}\text{Be}$  record on AICC2012 and AICC2023 chronologies between 778 and 760 ka BP.** Grey and blue  
 801 vertical bars indicate the age of the abrupt EDC  $^{10}\text{Be}$  peak termination respectively on AICC2012 (grey triangles) and  
 802 AICC2023 (blue circles) chronologies. The grey and blue horizontal squares correspond to AICC2012 and AICC2023 age  
 803 uncertainties ( $\pm 3$  and  $\pm 2.7$  ka respectively). The red vertical bar and horizontal square show the  $^{10}\text{Be}$  peak termination age and  
 804 its error (Giaccio et al., 2023).

805

## 806 Conclusions

807 In this study, we have established a new reference chronology for EDC ice core, AICC2023 covering the  
 808 last 800 kyr, that is consistent with the official GICC05 timescale over the last 60 kyr. A valuable update of the  
 809 chronology construction has been the compilation of chronological and glaciological information including new  
 810 age markers from recent high resolution measurements on the EDC ice core. As a result, the chronological  
 811 uncertainty is reduced from 2.5 kyr in AICC2012 (standard deviation of 995 years) to 1.8 kyr on average here  
 812 (standard deviation of 720 years). 90% of the new AICC2023 timescale is associated with an uncertainty lower  
 813 than 2 kyr, against only 60% in the AICC2012 chronology. First, the distinct orbital chronologies derived from  
 814 TAC,  $\delta^{18}\text{O}_{\text{atm}}$  and  $\delta\text{O}_2/\text{N}_2$  are coherent within their respective uncertainties except over three periods including  
 815 MIS 11 and MIS 19. Second, new  $\delta^{15}\text{N}$  measurements along with new sensitivity tests with the firm densification  
 816 model described by Bréant et al. (2017) and adapted for the EDC ice core provide the most plausible evolution of  
 817 LID at EDC over the last 800 kyr.

818 The majority of the age disparities observed between AICC2023 and AICC2012 chronologies are smaller  
 819 than 2.3 kyr, hence minor considering the average uncertainty of AICC2012 (2.5 kyr). Exceptions are significant  
 820 age shifts reaching 3.4, 3.8 and 5 kyr towards older ages respectively suggested over MIS 15, MIS 17 and MIS 19.  
 821 However, most of these age discrepancies lead to an improved coherency between the new EDC timescale and  
 822 independent absolute chronologies derived for other climate archives especially over the following periods: MIS  
 823 5, MIS 11 and MIS 19.



824 We have identified time intervals where building the chronology is more complicated such as TVI (from 540  
825 to 456 ka BP) and from 800 to 600 ka BP, corresponding to the lowermost section of the core and we would like  
826 to draw attention to the requirement for new measurements over these periods. In particular, the links between the  
827 variability of TAC and  $\delta O_2/N_2$  records and their orbital targets are not obvious over the 800 – 600 ka BP period  
828 (Fig. 1). This may be due to bad quality of the ice and/or diffusion of gases through the ice matrix (Bereiter et al.,  
829 2009). The imprecision of the signal may also be partially explained by the limited temporal resolution of the  
830 existing dataset in this deep section. To address these issues, highly resolved TAC and  $\delta O_2/N_2$  measurements are  
831 needed in the lowermost section of EDC ice core. In addition,  $\delta O_2/N_2$  from ice samples over the period covering  
832 TVI should also be analyzed to investigate the mismatch between old and new datasets (Fig. 1).

833 A final important aspect would be to further extend the Paleochrono dating experiment by implementing other  
834 ice cores such as Dome Fuji, WAIS (West Antarctic Ice Sheet) Divide and NEEM (North Greenland Eemian), for  
835 which a large amount of chronological and glaciological information is now available.

#### 836 **Author contribution**

837 Marie Bouchet wrote the manuscript with the contribution of all co-authors. Amaëlle Landais and Frédéric  
838 Parrenin contributed to the conceptualization of the study and the methodology. Measurements on the EDC ice  
839 core were performed at the LSCE by Antoine Grisart, Frédéric Prié, Roxanne Jacob and Elise Fourré. Emilie  
840 Capron, Dominique Raynaud, Vladimir Ya Lipenkov and Marie-France Loutre contributed to the collection,  
841 analysis and interpretation of the TAC record. Markus Leuenberger provided resources. The Krypton analysis was  
842 conducted by Wei Jiang, Florian Ritterbusch, Zheng-Tian Lu, Guo-Min Yang. Thomas Extier, Anders Svensson,  
843 Etienne Legrain and Patricia Martinerie contributed to the validation of the study.

#### 844 **Competing interests**

845 At least one of the authors is a member of the editorial board of *Climate of the Past*. The peer-review process was  
846 guided by an independent editor, and the authors have also no other competing interests to declare.

#### 847 **Acknowledgements**

848 The research leading to these results has received funding from the European Research Council under the European  
849 Union H2020 Programme (H2020/20192024)/ERC grant agreement no. 817493 (ERC ICORDA). Krypton  
850 analysis has been supported by the Innovation Program for Quantum Science and Technology 2021ZD0303101,  
851 and by the National Natural Science Foundation of China (41727901). Development of the Paleochrono model  
852 was funded by CNRS/INSU/LEFE projects IceChrono and CO2Role. EC and EL acknowledge the financial  
853 support from the French National Research Agency under the “Programme d’Investissements d’Avenir” (ANR-  
854 19-MPGA-0001), through the Make Our Planet Great Again HOTCLIM project as well as the financial support  
855 from the AXA Research Fund. We also acknowledge the assistance from the European Union FP5-EESD  
856 Programme grant agreement no. EVK2-CT-2000-00077 (EPICA), the French National Research Agency  
857 Programme “NEANDROOTS” (ANR-19-CE27-0011) and the French Polar Institute project no. 902  
858 (GLACIOLOGIE CONCORDIA). Our special thanks go to Markus Grimmer, Marcel Haeberli, Daniel  
859 Bagginstos, Jochen Schmitt, Matthias Baumgartner, Hubertus Fischer, Kenji Kawamura and Ikumi Oyabu for





860 sharing their thoughts and data, sustaining the discussion on the construction of new ice core age scales, and to  
861 Sébastien Nomade and Alison Pereira for providing advice and expertise in geochronology.

## 862 References

863 Andersen, K. K., Azuma, N., Barnola, J.-M., Bigler, M., Biscaye, P., Caillon, N., Chappellaz, J., Clausen, H. B.,  
864 Dahl-Jensen, D., Fischer, H., Flückiger, J., Fritzsche, D., Fujii, Y., Goto-Azuma, K., Grønvoold, K., Gundestrup,  
865 N. S., Hansson, M., Huber, C., Hvidberg, C. S., Johnsen, S. J., Jonsell, U., Jouzel, J., Kipfstuhl, S., Landais, A.,  
866 Leuenberger, M., Lorrain, R., Masson-Delmotte, V., Miller, H., Motoyama, H., Narita, H., Popp, T., Rasmussen,  
867 S. O., Raynaud, D., Rothlisberger, R., Ruth, U., Samyn, D., Schwander, J., Shoji, H., Siggard-Andersen, M.-L.,  
868 Steffensen, J. P., Stocker, T., Sveinbjörnsdóttir, A. E., Svensson, A., Takata, M., Tison, J.-L., Thorsteinsson, Th.,  
869 Watanabe, O., Wilhelms, F., White, J. W. C., and members, N. G. I. C. P.: High-resolution record of Northern  
870 Hemisphere climate extending into the last interglacial period, *Nature*, 431, 147–151,  
871 <https://doi.org/10.1038/nature02805>, 2004.

872 Andersen, K. K., Svensson, A., Johnsen, S. J., Rasmussen, S. O., Bigler, M., Röthlisberger, R., Ruth, U.,  
873 Siggaard-Andersen, M.-L., Peder Steffensen, J., Dahl-Jensen, D., Vinther, B. M., and Clausen, H. B.: The  
874 Greenland Ice Core Chronology 2005, 15–42ka. Part 1: constructing the time scale, *Quat Sci Rev*, 25, 3246–  
875 3257, <https://doi.org/https://doi.org/10.1016/j.quascirev.2006.08.002>, 2006.

876 Barker, S (2021): Planktic foraminiferal and Ice Rafted Debris (IRD) counts from ODP Site 983:  
877 <https://doi.pangaea.de/10.1594/PANGAEA.929721>, last access: 8 January 2023.

878 Arnaud, L., Barnola, J. M., and Duval, P.: Physical modeling of the densification of snow/firn and ice in the  
879 upper part of polar ice sheets, *Physics of the Ice Core Records*, 285–305, <http://hdl.handle.net/2115/32472>, 2000.

880 Augustin, L., Barbante, C., Barnes, P. R. F., Barnola, J. M., Bigler, M., Castellano, E., Cattani, O., Chappellaz,  
881 J., Dahl-Jensen, D., Delmonte, B., Dreyfus, G., Durand, G., Falourd, S., Fischer, H., Flückiger, J., Hansson, M.  
882 E., Huybrechts, P., Jugie, G., Johnsen, S. J., Jouzel, J., Kaufmann, P., Kipfstuhl, J., Lambert, F., Lipenkov, V.  
883 Y., Littot, G. C., Longinelli, A., Lorrain, R., Maggi, V., Masson-Delmotte, V., Miller, H., Mulvaney, R.,  
884 Oerlemans, J., Oerter, H., Orombelli, G., Parrenin, F., Peel, D. A., Petit, J. R., Raynaud, D., Ritz, C., Ruth, U.,  
885 Schwander, J., Siegenthaler, U., Souchez, R., Stauffer, B., Steffensen, J. P., Stenni, B., Stocker, T. F., Tabacco, I.  
886 E., Udisti, R., van de Wal, R. S. W., van den Broeke, M., Weiss, J., Wilhelms, F., Winther, J. G., Wolff, E. W.,  
887 and Zucchelli, M.: Eight glacial cycles from an Antarctic ice core, *Nature* 2004 429:6992, 429, 623–628,  
888 <https://doi.org/10.1038/nature02599>, 2004.

889 Baglin, C. M.: Nuclear Data Sheets for A = 81, *Nuclear Data Sheets*, 109, 2257–2437,  
890 <https://doi.org/10.1016/J.NDS.2008.09.001>, 2008.

891 BARNOLA, J. -M, PIMIANTA, P., RAYNAUD, D., and KOROTKEVICH, Y. S.: CO<sub>2</sub>-climate relationship as  
892 deduced from the Vostok ice core: a re-examination based on new measurements and on a re-evaluation of the  
893 air dating, *Tellus B*, 43, 83–90, <https://doi.org/10.1034/J.1600-0889.1991.T01-1-00002.X>, 1991.

894 Baumgartner, M., Kindler, P., Eicher, O., Floch, G., Schilt, A., Schwander, J., Spahni, R., Capron, E.,  
895 Chappellaz, J., Leuenberger, M., Fischer, H., and Stocker, T. F.: NGRIP CH<sub>4</sub> concentration from 120 to 10 kyr  
896 before present and its relation to a  $\delta^{15}N$  temperature reconstruction from the same ice core, *Clim. Past*, 10, 903–  
897 920, <https://doi.org/10.5194/CP-10-903-2014>, 2014.

898 Bazin, L., Landais, A., Lemieux-Dudon, B., Toyé Mahamadou Kele, H., Veres, D., Parrenin, F., Martinerie, P.,  
899 Ritz, C., Capron, E., Lipenkov, V., Loutre, M.-F., Raynaud, D., Vinther, B., Svensson, A., Rasmussen, S. O.,  
900 Severi, M., Blunier, T., Leuenberger, M., Fischer, H., Masson-Delmotte, V., Chappellaz, J., and Wolff, E.: An  
901 optimized multi-proxy, multi-site Antarctic ice and gas orbital chronology (AICC2012): 120–800 ka, *Clim. Past*,  
902 9, 1715–1731, <https://doi.org/10.5194/cp-9-1715-2013>, 2013.

903 Bazin, L., Landais, A., Capron, E., Masson-Delmotte, V., Ritz, C., Picard, G., Jouzel, J., Dumont, M.,  
904 Leuenberger, M., and Prié, F.: Phase relationships between orbital forcing and the composition of air trapped in  
905 Antarctic ice cores, *Clim. Past*, 12, 729–748, <https://doi.org/10.5194/cp-12-729-2016>, 2016.



- 906 Bender, M. L.: Orbital tuning chronology for the Vostok climate record supported by trapped gas composition,  
907 *Earth Planet. Sci. Lett.*, 204, 275–289, [https://doi.org/10.1016/S0012-821X\(02\)00980-9](https://doi.org/10.1016/S0012-821X(02)00980-9), 2002.
- 908 Bender, M. L., Barnett, B., Dreyfus, G., Jouzel, J., and Porcelli, D.: The contemporary degassing rate of 40Ar  
909 from the solid Earth, *PNAS*, 105, 8232–8237, <https://doi.org/10.1073/PNAS.0711679105>, 2008.
- 910 Bereiter, B., Schwander, J., Lüthi, D., and Stocker, T. F.: Change in CO<sub>2</sub> concentration and O<sub>2</sub>/N<sub>2</sub> ratio in ice  
911 cores due to molecular diffusion, *Geophys Res Lett*, 36, <https://doi.org/10.1029/2008GL036737>, 2009.
- 912 Berger, AndréL.: Long-Term Variations of Daily Insolation and Quaternary Climatic Changes, *JAS*, 35, 2362–  
913 2367, [https://doi.org/https://doi.org/10.1175/1520-0469\(1978\)035<2362:LTVODI>2.0.CO;2](https://doi.org/https://doi.org/10.1175/1520-0469(1978)035<2362:LTVODI>2.0.CO;2), 1978.
- 914 Berger, B., Crucifix, M., Hodell, D. A., Mangili, C., McManus, J. F., Otto-Bliesner, B., Pol, K., Raynaud, D.,  
915 Skinner, L. C., Tzedakis, P. C., Wolff, E. W., Yin, Q. Z., Abe-Ouchi, A., Barbante, C., Brovkin, V., Cacho, I.,  
916 Capron, E., Ferretti, P., Ganopolski, A., Grimalt, J. O., Hönlisch, B., Kawamura, K. A., Landais, A., Margari, V.,  
917 Martrat, B., Masson-Delmotte, V., Mokeddem, Z., Parrenin, F., Prokopenko, A. A., Rashid, H., Schulz, M., and  
918 Vazquez Riveiros, N.: Interglacials of the last 800,000 years, *Rev. Geophys.*, 54, 162–219,  
919 <https://doi.org/10.1002/2015RG000482>, 2016.
- 920 Boch, R., Cheng, H., Spötl, C., Edwards, R. L., Wang, X., and Häuselmann, Ph.: NALPS: a precisely dated  
921 European climate record 120–60 ka, *Clim. Past*, 7, 1247–1259, <https://doi.org/10.5194/cp-7-1247-2011>, 2011.
- 922 Bréant, C., Martinerie, P., Orsi, A., Arnaud, L., and Landais, A.: Modelling firn thickness evolution during the  
923 last deglaciation: constraints on sensitivity to temperature and impurities, *Clim. Past*, 13, 833–853,  
924 <https://doi.org/10.5194/cp-13-833-2017>, 2017.
- 925 Bréant, C., Landais, A., Orsi, A., Martinerie, P., Extier, T., Prié, F., Stenni, B., Jouzel, J., Masson-Delmotte, V.,  
926 and Leuenberger, M.: Unveiling the anatomy of Termination 3 using water and air isotopes in the Dome C ice  
927 core, East Antarctica, *Quat. Sci. Rev.*, 211, 156–165, <https://doi.org/10.1016/J.QUASCIREV.2019.03.025>, 2019.
- 928 Buizert, C.: The Ice Core Gas Age-Ice Age Difference as a Proxy for Surface Temperature, *Geophys. Res. Lett.*,  
929 48, e2021GL094241, <https://doi.org/10.1029/2021GL094241>, 2021.
- 930 Buizert, C., Sowers, T., and Blunier, T.: Assessment of diffusive isotopic fractionation in polar firn, and  
931 application to ice core trace gas records, *Earth Planet. Sci. Lett.*, 361, 110–119,  
932 <https://doi.org/10.1016/J.EPSL.2012.11.039>, 2013.
- 933 Buizert, C., Bagginstos, D., Jiang, W., Purtschert, R., Petrenko, V. V., Lu, Z. T., Müller, P., Kuhl, T., Lee, J.,  
934 Severinghaus, J. P., and Brook, E. J.: Radiometric 81Kr dating identifies 120,000-year-old ice at Taylor Glacier,  
935 Antarctica, *PNAS*, 111, 6876–6881,  
936 [https://doi.org/10.1073/PNAS.1320329111/SUPPL\\_FILE/PNAS.1320329111.SD01.XLS](https://doi.org/10.1073/PNAS.1320329111/SUPPL_FILE/PNAS.1320329111.SD01.XLS), 2014.
- 937 Caillon, N., Jouzel, J., Severinghaus, J. P., Chappellaz, J., and Blunier, T.: A novel method to study the phase  
938 relationship between Antarctic and Greenland climate, *Geophys. Res. Lett.*, 30,  
939 <https://doi.org/10.1029/2003GL017838>, 2003.
- 940 Capron, E., Landais, A., Chappellaz, J., Schilt, A., Buiron, D., Dahl-Jensen, D., Johnsen, S. J., Jouzel, J.,  
941 Lemieux-Dudon, B., Loulergue, L., Leuenberger, M., Masson-Delmotte, V., Meyer, H., Oerter, H., and Stenni,  
942 B.: Millennial and sub-millennial scale climatic variations recorded in polar ice cores over the last glacial period,  
943 *Climat. Past*, 6, 345–365, <https://doi.org/10.5194/CP-6-345-2010>, 2010.
- 944 Capron, E., Landais, A., Chappellaz, J., Buiron, D., Fischer, H., Johnsen, S. J., Jouzel, J., Leuenberger, M.,  
945 Masson-Delmotte, V., and Stocker, T. F.: A global picture of the first abrupt climatic event occurring during the  
946 last glacial inception, *Geophys. Res. Lett.*, 39, <https://doi.org/10.1029/2012GL052656>, 2012a.
- 947 Capron, E., Landais, A., Chappellaz, J., Buiron, D., Fischer, H., Johnsen, S. J., Jouzel, J., Leuenberger, M.,  
948 Masson-Delmotte, V., and Stocker, T. F.: A global picture of the first abrupt climatic event occurring during the  
949 last glacial inception, *Geophys. Res. Lett.*, 39, <https://doi.org/10.1029/2012GL052656>, 2012b.
- 950 Capron, E., Landais, A., Buiron, D., Cauquoin, A., Chappellaz, J., Debret, M., Jouzel, J., Leuenberger, M.,  
951 Martinerie, P., Masson-Delmotte, V., Mulvaney, R., Parrenin, F., and Prié, F.: Glacial-interglacial dynamics of



- 952 Antarctic firn columns: Comparison between simulations and ice core air- $\delta^{15}\text{N}$  measurements, *Clim. Past*, 9,  
953 983–999, <https://doi.org/10.5194/CP-9-983-2013>, 2013.
- 954 Cheng, H., Edwards, R. L., Sinha, A., Spötl, C., Yi, L., Chen, S., Kelly, M., Kathayat, G., Wang, X., Li, X.,  
955 Kong, X., Wang, Y., Ning, Y., and Zhang, H.: The Asian monsoon over the past 640,000 years and ice age  
956 terminations, *Nature*, 534, 640–646, <https://doi.org/10.1038/nature18591>, 2016.
- 957 Columbu, A., Drysdale, R., Capron, E., Woodhead, J., De Waele, J., Sanna, L., Hellstrom, J., and Bajo, P.: Early  
958 last glacial intra-interstadial climate variability recorded in a Sardinian speleothem, *Quat. Sci. Rev.*, 169, 391–  
959 397, <https://doi.org/10.1016/J.QUASCIREV.2017.05.007>, 2017.
- 960 Crotti, I., Landais, A., Stenni, B., Bazin, L., Parrenin, F., Frezzotti, M., Ritterbusch, F., Lu, Z. T., Jiang, W.,  
961 Yang, G. M., Fourné, E., Orsi, A., Jacob, R., Minster, B., Prié, F., Dreossi, G., and Barbante, C.: An extension of  
962 the TALDICE ice core age scale reaching back to MIS 10.1, *Quat. Sci. Rev.*, 266, 107078,  
963 <https://doi.org/10.1016/J.QUASCIREV.2021.107078>, 2021.
- 964 Dansgaard, W. and Johnsen, S. J.: A Flow Model and a Time Scale for the Ice Core from Camp Century,  
965 Greenland, *J. Glaciol.*, 8, 215–223, <https://doi.org/10.3189/S0022143000031208>, 1969.
- 966 Dong, X. Z., Ritterbusch, F., Chu, Y. Q., Gu, J. Q., Hu, S. M., Jiang, W., Lu, Z. T., Yang, G. M., and Zhao, L.:  
967 Dual Separation of Krypton and Argon from Environmental Samples for Radioisotope Dating, *Anal. Chem.*, 91,  
968 13576–13581,  
969 [https://doi.org/10.1021/ACS.ANALCHEM.9B02716/ASSET/IMAGES/MEDIUM/AC9B02716\\_0004.GIF](https://doi.org/10.1021/ACS.ANALCHEM.9B02716/ASSET/IMAGES/MEDIUM/AC9B02716_0004.GIF),  
970 2019.
- 971 Dreyfus, G. B., Parrenin, F., Lemieux-Dudon, B., Durand, G., Masson-Delmotte, V., Jouzel, J., Barnola, J. M.,  
972 Panno, L., Spahni, R., Tisserand, A., Siegenthaler, U., and Leuenberger, M.: Anomalous flow below 2700 m in  
973 the EPICA Dome C ice core detected using  $\delta^{18}\text{O}$  of atmospheric oxygen measurements, *Clim. Past*, 3, 341–353,  
974 <https://doi.org/10.5194/CP-3-341-2007>, 2007.
- 975 Dreyfus, G. B., Raisbeck, G. M., Parrenin, F., Jouzel, J., Guyodo, Y., Nomade, S., and Mazaud, A.: An ice core  
976 perspective on the age of the Matuyama–Brunhes boundary, *Earth Planet. Sci. Lett.*, 274, 151–156,  
977 <https://doi.org/10.1016/J.EPSL.2008.07.008>, 2008.
- 978 Dreyfus, G. B., Jouzel, J., Bender, M. L., Landais, A., Masson-Delmotte, V., and Leuenberger, M.: Firn  
979 processes and  $\delta^{15}\text{N}$ : potential for a gas-phase climate proxy, *Quat. Sci. Rev.*, 29, 28–42,  
980 <https://doi.org/10.1016/j.quascirev.2009.10.012>, 2010.
- 981 Epifanio, J. A., Brook, E. J., Buizert, C., Edwards, J. S., Sowers, T. A., Kahle, E. C., Severinghaus, J. P., Steig,  
982 E. J., Winski, D. A., Osterberg, E. C., Fudge, T. J., Aydin, M., Hood, E., Kalk, M., Kreutz, K. J., Ferris, D. G.,  
983 and Kennedy, J. A.: The SP19 chronology for the South Pole Ice Core - Part 2: Gas chronology,  $\Delta\text{age}$ , and  
984 smoothing of atmospheric records, *Clim. Past*, 16, 2431–2444, <https://doi.org/10.5194/CP-16-2431-2020>, 2020.
- 985 Extier, T., Landais, A., Bréant, C., Prié, F., Bazin, L., Dreyfus, G., Roche, D. M., and Leuenberger, M.: On the  
986 use of  $\delta^{18}\text{O}_{\text{atm}}$  for ice core dating, *Quat. Sci. Rev.*, 185, 244–257,  
987 <https://doi.org/10.1016/J.QUASCIREV.2018.02.008>, 2018a.
- 988 Extier, T., Landais, A., Bréant, C., Prié, F., Bazin, L., Dreyfus, G., Roche, D. M., and Leuenberger, M. C.:  
989  $\delta^{18}\text{O}_{\text{atm}}$  records between 100–800 ka from EPICA Dome C ice core, PANGAEA,  
990 <https://doi.org/10.1594/PANGAEA.887323>, 2018b.
- 991 Extier, T., Landais, A., Bréant, C., Prié, F., Bazin, L., Dreyfus, G., Roche, D. M., and Leuenberger, M. C.:  
992  $\delta^{18}\text{O}_2/\text{N}_2$  records between 100–800 ka from EPICA Dome C ice core, PANGAEA,  
993 <https://doi.org/10.1594/PANGAEA.887326>, 2018c.
- 994 Freitag, J., Kipfstuhl, S., Laepple, T., and Wilhelms, F.: Impurity-controlled densification: a new model for  
995 stratified polar firn, *J. Glaciol.*, 59, 1163–1169, <https://doi.org/10.3189/2013JOG13J042>, 2013.
- 996 Fujita, S., Parrenin, F., Severi, M., Motoyama, H., and Wolff, E. W.: Volcanic synchronization of Dome Fuji and  
997 Dome C Antarctic deep ice cores over the past 216 kyr, *Clim. Past*, 11, 1395–1416, <https://doi.org/10.5194/CP-11-1395-2015>, 2015.



- 1999 Giaccio, B., Zanchetta, G., Galli, P., Nomade, S., Regattieri, E., and Sagnotti, L.: The Quaternary evolution of  
1000 Sulmona basin, central Italy, <https://inquareoma2023.org/wp-content/uploads/2022/01/5-Post.pdf>, last access: 22  
1001 May 2023.
- 1002 Goujon, C., Barnola, J. M., and Ritz, C.: Modeling the densification of polar firn including heat diffusion:  
1003 Application to close-off characteristics and gas isotopic fractionation for Antarctica and Greenland sites, *J.*  
1004 *Geophys. Res. Atmos.*, 108, 4792, <https://doi.org/10.1029/2002JD003319>, 2003.
- 1005 Grachev, A. M. and Severinghaus, J. P.: Determining the Thermal Diffusion Factor for  $^{40}\text{Ar}/^{36}\text{Ar}$  in Air To Aid  
1006 Paleoreconstruction of Abrupt Climate Change, *J. Phys. Chem.*, 107, 4636–4642,  
1007 <https://doi.org/10.1021/JP027817U>, 2003.
- 1008 Grisart, A.: Étude à haute résolution des cycles hydrologiques et climatiques à partir d'une carotte de glace  
1009 d'Antarctique avec un focus sur les déglaciations, Ph.D., LSCE, <https://theses.hal.science/tel-04042459>, 2023.
- 1010 Heaton, T. J., Bard, E., Ramsey, C. B., Butzin, M., Köhler, P., Muscheler, R., Reimer, P. J., and Wacker, L.:  
1011 Radiocarbon: A key tracer for studying Earth's dynamo, climate system, carbon cycle, and Sun, *Science*, 374,  
1012 <https://doi.org/10.1126/SCIENCE.ABD7096>, 2021.
- 1013 Hörhold, M. W., Laepple, T., Freitag, J., Bigler, M., Fischer, H., and Kipfstuhl, S.: On the impact of impurities  
1014 on the densification of polar firn, *Earth Planet. Sci. Lett.*, 325–326, 93–99,  
1015 <https://doi.org/10.1016/J.EPSL.2011.12.022>, 2012.
- 1016 Jouzel, J., Hoffmann, G., Parrenin, F., and Waelbroeck, C.: Atmospheric oxygen 18 and sea-level changes, *Quat.*  
1017 *Sci. Rev.*, 21, 307–314, [https://doi.org/10.1016/S0277-3791\(01\)00106-8](https://doi.org/10.1016/S0277-3791(01)00106-8), 2002.
- 1018 Jouzel, J., Masson-Delmotte, V., Cattani, O., Dreyfus, G., Falourd, S., Hoffmann, G., Minster, B., Nouet, J.,  
1019 Barnola, J. M., Chappellaz, J., Fischer, H., Gallet, J. C., Johnsen, S., Leuenberger, M., Loulergue, L., Luethi, D.,  
1020 Oerter, H., Parrenin, F., Raisbeck, G., Raynaud, D., Schilt, A., Schwander, J., Selmo, E., Souchez, R., Spahni,  
1021 R., Stauffer, B., Steffensen, J. P., Stenni, B., Stocker, T. F., Tison, J. L., Werner, M., and Wolff, E. W.: Orbital  
1022 and millennial antarctic climate variability over the past 800,000 years, *Science*, 317, 793–796,  
1023 <https://doi.org/10.1126/SCIENCE.1141038>, 2007.
- 1024 Kawamura, K., Parrenin, F., Lisiecki, L., Uemura, R., Vimeux, F., Severinghaus, J. P., Hutterli, M. A.,  
1025 Nakazawa, T., Aoki, S., Jouzel, J., Raymo, M. E., Matsumoto, K., Nakata, H., Motoyama, H., Fujita, S., Goto-  
1026 Azuma, K., Fujii, Y., and Watanabe, O.: Northern Hemisphere forcing of climatic cycles in Antarctica over the  
1027 past 360,000 years, *Nature*, 448, 912–916, <https://doi.org/10.1038/nature06015>, 2007.
- 1028 Landais, A., Chappellaz, J., Delmotte, M., Jouzel, J., Blunier, T., Bourg, C., Caillon, N., Cherrier, S., Malaizé,  
1029 B., Masson-Delmotte, V., Raynaud, D., Schwander, J., and Steffensen, J. P.: A tentative reconstruction of the  
1030 last interglacial and glacial inception in Greenland based on new gas measurements in the Greenland Ice Core  
1031 Project (GRIP) ice core, *J. Geophys. Res. Atmos.*, 108, <https://doi.org/10.1029/2002JD003147>, 2003.
- 1032 Landais, A., Barnola, J. M., Kawamura, K., Caillon, N., Delmotte, M., Van Ommen, T., Dreyfus, G., Jouzel, J.,  
1033 Masson-Delmotte, V., Minster, B., Freitag, J., Leuenberger, M., Schwander, J., Huber, C., Etheridge, D., and  
1034 Morgan, V.: Firn-air  $\delta^{15}\text{N}$  in modern polar sites and glacial–interglacial ice: a model–data mismatch during  
1035 glacial periods in Antarctica?, *Quat. Sci. Rev.*, 25, 49–62, <https://doi.org/10.1016/J.QUASCIREV.2005.06.007>,  
1036 2006.
- 1037 Landais, A., Dreyfus, G., Capron, E., Masson-Delmotte, V., Sanchez-Goñi, M. F., Desprat, S., Hoffmann, G.,  
1038 Jouzel, J., Leuenberger, M., and Johnsen, S.: What drives the millennial and orbital variations of  $\delta^{18}\text{O}_{\text{atm}}$ ?  
1039 *Quat. Sci. Rev.*, 29, 235–246, <https://doi.org/10.1016/J.QUASCIREV.2009.07.005>, 2010.
- 1040 Landais, A., Dreyfus, G., Capron, E., Pol, K., Loutre, M. F., Raynaud, D., Lipenkov, V. Y., Arnaud, L., Masson-  
1041 Delmotte, V., Paillard, D., Jouzel, J., and Leuenberger, M.: Towards orbital dating of the EPICA Dome C ice  
1042 core using  $\delta\text{O} 2/\text{N} 2$ , *Clim. Past*, 8, 191–203, <https://doi.org/10.5194/CP-8-191-2012>, 2012.
- 1043 Landais, A., Stenni, B., Masson-Delmotte, V., Jouzel, J., Cauquoin, A., Fourré, E., Minster, B., Selmo, E.,  
1044 Extier, T., Werner, M., Vimeux, F., Uemura, R., Crotti, I., and Grisart, A.: Interglacial Antarctic–Southern  
1045 Ocean climate decoupling due to moisture source area shifts, *Nature Geoscience*, 14, 918–923,  
1046 <https://doi.org/10.1038/s41561-021-00856-4>, 2021.



- 1047 Lascu, I., Feinberg, J. M., Dorale, J. A., Cheng, H., and Edwards, R. L.: Age of the Laschamp excursion  
1048 determined by U-Th dating of a speleothem geomagnetic record from North America, *Geology*, 44, 139–142,  
1049 <https://doi.org/10.1130/G37490.1>, 2016.
- 1050 Laskar, J., Robutel, P., Joutel, F., Gastineau, M., Correia, A. C. M., and Levrard, B.: A long-term numerical  
1051 solution for the insolation quantities of the Earth, *Astron. Astrophys.*, 428, 261–285,  
1052 <https://doi.org/10.1051/0004-6361:20041335>, 2004.
- 1053 Laskar, J., Fienga, A., Gastineau, M., and Manche, H.: La2010: a new orbital solution for the long-term motion  
1054 of the Earth, *Astron. Astrophys.*, 532, A89, <https://doi.org/10.1051/0004-6361/201116836>, 2011.
- 1055 Lemieux-Dudon, B., Blayo, E., Petit, J. R., Waelbroeck, C., Svensson, A., Ritz, C., Barnola, J. M., Narcisi, B.  
1056 M., and Parrenin, F.: Consistent dating for Antarctic and Greenland ice cores, *Quat. Sci. Rev.*, 29, 8–20,  
1057 <https://doi.org/10.1016/J.QUASCIREV.2009.11.010>, 2010.
- 1058 Lemieux-Dudon, B., Bazin, L., Landais, A., Toyé Mahamadou Kele, H., Guillevic, M., Kindler, P., Parrenin, F.,  
1059 and Martinerie, P.: Implementation of counted layers for coherent ice core chronology, *Clim. Past*, 11, 959–978,  
1060 <https://doi.org/10.5194/CP-11-959-2015>, 2015.
- 1061 Lipenkov, V., Candaudap, F., Ravoire, J., Dulac, E., and Raynaud, D.: A new device for the measurement of air  
1062 content in polar ice, *J. Glaciol.*, 41, 423–429, <https://doi.org/10.3189/S0022143000016294>, 1995.
- 1063 Lipenkov, V. Y., Raynaud, D., Loutre, M. F., and Duval, P.: On the potential of coupling air content and O<sub>2</sub>/N<sub>2</sub>  
1064 from trapped air for establishing an ice core chronology tuned on local insolation, *Quat. Sci. Rev.*, 30, 3280–  
1065 3289, <https://doi.org/10.1016/J.QUASCIREV.2011.07.013>, 2011.
- 1066 Lu, Z. T., Schlosser, P., Smethie, W. M., Sturchio, N. C., Fischer, T. P., Kennedy, B. M., Purtschert, R.,  
1067 Severinghaus, J. P., Solomon, D. K., Tanhua, T., and Yokochi, R.: Tracer applications of noble gas radionuclides  
1068 in the geosciences, *Earth Sci. Rev.*, 138, 196–214, <https://doi.org/10.1016/J.EARSCIREV.2013.09.002>, 2014.
- 1069 Moseley, G. E., Spötl, C., Brandstätter, S., Erhardt, T., Luetscher, M., and Lawrence Edwards, R.: NALPS19:  
1070 Sub-orbital-scale climate variability recorded in northern Alpine speleothems during the last glacial period,  
1071 *Clim. Past*, 16, 29–50, <https://doi.org/10.5194/CP-16-29-2020>, 2020.
- 1072 Nehrbass-Ahles, C., Shin, J., Schmitt, J., Bereiter, B., Joos, F., Schilt, A., Schmidely, L., Silva, L., Teste, G.,  
1073 Grilli, R., Chappellaz, J., Hodell, D., Fischer, H., and Stocker, T. F.: Abrupt CO<sub>2</sub> release to the atmosphere  
1074 under glacia and early interglacial climate conditions, *Science*, 369, 1000–1005,  
1075 [https://doi.org/10.1126/SCIENCE.AAY8178/SUPPL\\_FILE/AAY8178\\_TABLES2.XLSX](https://doi.org/10.1126/SCIENCE.AAY8178/SUPPL_FILE/AAY8178_TABLES2.XLSX), 2020.
- 1076 Oyabu, I., Kawamura, K., Buizert, C., Parrenin, F., Orsi, A., Kitamura, K., Aoki, S., and Nakazawa, T.: The  
1077 Dome Fuji ice core DF2021 chronology (0–207 kyr BP), *Quat. Sci. Rev.*, 294, 107754,  
1078 <https://doi.org/10.1016/J.QUASCIREV.2022.107754>, 2022.
- 1079 Parrenin, F., Rémy, F., Ritz, C., Siebert, M. J., and Jouzel, J.: New modeling of the Vostok ice flow line and  
1080 implication for the glaciological chronology of the Vostok ice core, *J. Geophys. Res. Atmos.*, 109, 20102,  
1081 <https://doi.org/10.1029/2004JD004561>, 2004.
- 1082 Parrenin, F., Dreyfus, G., Durand, G., Fujita, S., Gagliardini, O., Gillet, F., Jouze, J., Kawamura, K., Lhomme,  
1083 N., Masson-Delmotte, V., Ritz, C., Schwander, J., Shoji, H., Uemura, R., Watanabe, O., and Yoshida, N.: 1-D-  
1084 ice flow modelling at EPICA Dome C and Dome Fuji, East Antarctica, *Clim. Past*, 3, 243–259,  
1085 <https://doi.org/10.5194/CP-3-243-2007>, 2007a.
- 1086 Parrenin, F., Barnola, J.-M., Beer, J., Blunier, T., Castellano, E., Chappellaz, J., Dreyfus, G., Fischer, H., Fujita,  
1087 S., Jouzel, J., Kawamura, K., Lemieux-Dudon, B., Loulergue, L., Masson-Delmotte, V., Narcisi, B., Petit, J.-R.,  
1088 Raisbeck, G., Raynaud, D., Ruth, U., Schwander, J., Severi, M., Spahni, R., Steffensen, J. P., Svensson, A.,  
1089 Udisti, R., Waelbroeck, C., and Wolff, E.: The EDC3 chronology for the EPICA Dome C ice core, *Clim. Past*, 3,  
1090 485–497, <https://doi.org/10.5194/cp-3-485-2007>, 2007b.
- 1091 Parrenin, F., Barker, S., Blunier, T., Chappellaz, J., Jouzel, J., Landais, A., Masson-Delmotte, V., Schwander, J.,  
1092 and Veres, D.: On the gas-ice depth difference ( $\Delta$ depth) along the EPICA Dome C ice core, *Clim. Past*, 8, 1239–  
1093 1255, <https://doi.org/10.5194/CP-8-1239-2012>, 2012.



- 1094 Parrenin, F., Bazin, L., Capron, E., Landais, A., Lemieux-Dudon, B., Masson-Delmotte, V., Parrenin, F., Bazin,  
1095 L., Capron, E., Landais, A., Lemieux-Dudon, B., and Masson-Delmotte, V.: IceChrono1: a probabilistic model  
1096 to compute a common and optimal chronology for several ice cores, *Geosci. Model. Dev.*, 8, 1473–1492,  
1097 <https://doi.org/10.5194/GMD-8-1473-2015>, 2015.
- 1098 Parrenin, F., Bazin, L., Capron, E., Landais, A., Lemieux-Dudon, B., and Masson-Delmotte, V.: IceChrono1 : un  
1099 modèle probabiliste pour calculer une chronologie commune et optimale pour plusieurs carottes de glace,  
1100 *Quaternaire*, 28, 179–184, <https://doi.org/10.4000/QUATERNAIRE.8121>, 2017.
- 1101 Parrenin, F., Bazin, L., Buizert, C., Capron, E., Chowdry Beeman, J., Corrick, E., Drysdale, R., Kawamura, K.,  
1102 Landais, A., Mulvaney, R., Oyabu, I., and Rasmussen, S.: The Paleochrono probabilistic model to derive a  
1103 consistent chronology for several paleoclimatic sites, *EGUGA*, EGU21-822,  
1104 <https://doi.org/10.5194/EGUSPHERE-EGU21-822>, 2021.
- 1105 Petit, J. R., Jouzel, J., Raynaud, D., Barkov, N. I., Barnola, J. M., Basile, I., Bender, M., Chappellaz, J., Davis,  
1106 M., Delaygue, G., Delmotte, M., Kotiyakov, V. M., Legrand, M., Lipenkov, V. Y., Lorius, C., Pépin, L., Ritz,  
1107 C., Saltzman, E., and Stievenard, M.: Climate and atmospheric history of the past 420,000 years from the Vostok  
1108 ice core, Antarctica, *Nature*, 399, 429–436, <https://doi.org/10.1038/20859>, 1999.
- 1109 Pimienta, P. and Duval, P.: RATE CONTROLLING PROCESSES IN THE CREEP OF POLAR GLACIER ICE  
1110 CONTROLLING PROCESSES IN THE CREEP OF POLAR GLACIER ICE, *J. phys., Colloq.*, 48,  
1111 <https://doi.org/10.1051/jphyscol:1987134i>, 1987.
- 1112 Raisbeck, G. M., Yiou, F., Jouzel, J., and Stocker, T. F.: Direct north-south synchronization of abrupt climate  
1113 change record in ice cores using Beryllium 10, *Clim. Past*, 3, 541–547, <https://doi.org/10.5194/CP-3-541-2007>,  
1114 2007.
- 1115 Raisbeck, G. M., Cauquoin, A., Jouzel, J., Landais, A., Petit, J. R., Lipenkov, V. Y., Beer, J., Synal, H. A.,  
1116 Oerter, H., Johnsen, S. J., Steffensen, J. P., Svensson, A., and Yiou, F.: An improved north-south  
1117 synchronization of ice core records around the 41kyr 10Be peak, *Clim. Past*, 13, 217–229,  
1118 <https://doi.org/10.5194/CP-13-217-2017>, 2017.
- 1119 Raynaud, D., Lipenkov, V., Lemieux-Dudon, B., Duval, P., Loutre, M. F., and Lhomme, N.: The local insolation  
1120 signature of air content in Antarctic ice. A new step toward an absolute dating of ice records, *Earth Planet. Sci.*  
1121 *Lett.*, 261, 337–349, <https://doi.org/10.1016/J.EPSL.2007.06.025>, 2007.
- 1122 Reutenauer, C., Landais, A., Blunier, T., Bréant, C., Kageyama, M., Woillez, M. N., Risi, C., Mariotti, V., and  
1123 Braconnot, P.: Quantifying molecular oxygen isotope variations during a Heinrich stadial, *Clim. Past*, 11, 1527–  
1124 1551, <https://doi.org/10.5194/CP-11-1527-2015>, 2015.
- 1125 Sánchez Goñi, M. F., Landais, A., Fletcher, W. J., Naughton, F., Desprat, S., and Duprat, J.: Contrasting impacts  
1126 of Dansgaard–Oeschger events over a western European latitudinal transect modulated by orbital parameters,  
1127 *Quat. Sci. Rev.*, 27, 1136–1151, <https://doi.org/10.1016/J.QUASCIREV.2008.03.003>, 2008.
- 1128 Severinghaus, J. P., Bender, M. L., Keeling, R. F., and Broecker, W. S.: Fractionation of soil gases by diffusion  
1129 of water vapor, gravitational settling, and thermal diffusion, *Geochim. Cosmochim. Acta*, 60, 1005–1018,  
1130 [https://doi.org/10.1016/0016-7037\(96\)00011-7](https://doi.org/10.1016/0016-7037(96)00011-7), 1996.
- 1131 Shackleton, N. J.: The 100,000-year ice-age cycle identified and found to lag temperature, carbon dioxide, and  
1132 orbital eccentricity, *Science*, 289, 1897–1902, <https://doi.org/10.1126/SCIENCE.289.5486.1897>, 2000.
- 1133 Sigl, M., Fudge, T. J., Winstrup, M., Cole-Dai, J., Ferris, D., McConnell, J. R., Taylor, K. C., Welten, K. C.,  
1134 Woodruff, T. E., Adolphi, F., Bisiaux, M., Brook, E. J., Buizert, C., Caffee, M. W., Dunbar, N. W., Edwards, R.,  
1135 Geng, L., Iverson, N., Koffman, B., Layman, L., Maselli, O. J., McGwire, K., Muscheler, R., Nishizumi, K.,  
1136 Pasteris, D. R., Rhodes, R. H., and Sowers, T. A.: The WAIS Divide deep ice core WD2014 chronology – Part 2:  
1137 Annual-layer counting (0–31 ka BP), *Clim. Past*, 12, 769–786, <https://doi.org/10.5194/cp-12-769-2016>, 2016.
- 1138 Suwa, M. and Bender, M. L.: Chronology of the Vostok ice core constrained by O<sub>2</sub>/N<sub>2</sub> ratios of occluded air,  
1139 and its implication for the Vostok climate records, *Quat. Sci. Rev.*, 27, 1093–1106,  
1140 <https://doi.org/10.1016/J.QUASCIREV.2008.02.017>, 2008.



- 1141 Svensson, A., Andersen, K. K., Bigler, M., Clausen, H. B., Dahl-Jensen, D., Davies, S. M., Johnsen, S. J.,  
1142 Muscheler, R., Parrenin, F., Rasmussen, S. O., Röthlisberger, R., Seierstad, I., Steffensen, J. P., and Vinther, B.  
1143 M.: A 60 000 year Greenland stratigraphic ice core chronology, *Clim. Past*, 4, 47–57,  
1144 <https://doi.org/10.5194/CP-4-47-2008>, 2008.
- 1145 Svensson, A., Bigler, M., Blunier, T., Clausen, H. B., Dahl-Jensen, D., Fischer, H., Fujita, S., Goto-Azuma, K.,  
1146 Johnsen, S. J., Kawamura, K., Kipfstuhl, S., Kohno, M., Parrenin, F., Popp, T., Rasmussen, S. O., Schwander, J.,  
1147 Seierstad, I., Severi, M., Steffensen, J. P., Udisti, R., Uemura, R., Vallelonga, P., Vinther, B. M., Wegner, A.,  
1148 Wilhelms, F., and Winstrup, M.: Direct linking of Greenland and Antarctic ice cores at the Toba eruption (74 ka  
1149 BP), *Clim. Past*, 9, 749–766, <https://doi.org/10.5194/CP-9-749-2013>, 2013.
- 1150 Svensson, A., Dahl-Jensen, D., Steffensen, J. P., Blunier, T., Rasmussen, S. O., Vinther, B. M., Vallelonga, P.,  
1151 Capron, E., Gkinis, V., Cook, E., Kjær, H. A., Muscheler, R., Kipfstuhl, S., Wilhelms, F., Stocker, T. F., Fischer,  
1152 H., Adolphi, F., Erhardt, T., Sigl, M., Landais, A., Parrenin, F., Buizert, C., McConnell, J. R., Severi, M.,  
1153 Mulvaney, R., and Bigler, M.: Bipolar volcanic synchronization of abrupt climate change in Greenland and  
1154 Antarctic ice cores during the last glacial period, *Clim. Past*, 16, 1565–1580, [https://doi.org/10.5194/cp-16-1565-](https://doi.org/10.5194/cp-16-1565-2020)  
1155 2020, 2020.
- 1156 Tian, L., Ritterbusch, F., Gu, J. Q., Hu, S. M., Jiang, W., Lu, Z. T., Wang, D., and Yang, G. M.: 81Kr Dating at  
1157 the Guliya Ice Cap, Tibetan Plateau, *Geophys. Res. Lett.*, 46, 6636–6643,  
1158 <https://doi.org/10.1029/2019GL082464>, 2019.
- 1159 Uemura, R., Motoyama, H., Masson-Delmotte, V., Jouzel, J., Kawamura, K., Goto-Azuma, K., Fujita, S.,  
1160 Kuramoto, T., Hirabayashi, M., Miyake, T., Ohno, H., Fujita, K., Abe-Ouchi, A., Iizuka, Y., Horikawa, S.,  
1161 Igarashi, M., Suzuki, K., Suzuki, T., and Fujii, Y.: Asynchrony between Antarctic temperature and CO<sub>2</sub>  
1162 associated with obliquity over the past 720,000 years, *Nature Communications*, 9, 1–11,  
1163 <https://doi.org/10.1038/s41467-018-03328-3>, 2018.
- 1164 Veres, D., Bazin, L., Landais, A., Toyé Mahamadou Kele, H., Lemieux-Dudon, B., Parrenin, F., Martinerie, P.,  
1165 Blayo, E., Blunier, T., Capron, E., Chappellaz, J., Rasmussen, S. O., Severi, M., Svensson, A., Vinther, B., and  
1166 Wolff, E. W.: The Antarctic ice core chronology (AICC2012): an optimized multi-parameter and multi-site  
1167 dating approach for the last 120 thousand years, *Clim. Past*, 9, 1733–1748, [https://doi.org/10.5194/cp-9-1733-](https://doi.org/10.5194/cp-9-1733-2013)  
1168 2013, 2013.
- 1169 Wolff, E. W., Chappellaz, J., Blunier, T., Rasmussen, S. O., and Svensson, A.: Millennial-scale variability  
1170 during the last glacial: The ice core record, *Quat. Sci. Rev.*, 29, 2828–2838,  
1171 <https://doi.org/10.1016/J.QUASCIREV.2009.10.013>, 2010.
- 1172 Yan, Y., Bender, M. L., Brook, E. J., Clifford, H. M., Kemeny, P. C., Kurbatov, A. v., Mackay, S., Mayewski, P.  
1173 A., Ng, J., Severinghaus, J. P., and Higgins, J. A.: Two-million-year-old snapshots of atmospheric gases from  
1174 Antarctic ice, *Nature*, 574, 663–666, <https://doi.org/10.1038/s41586-019-1692-3>, 2019.
- 1175 Yiou, F., Raisbeck, G. M., Baumgartner, S., Beer, J., Hammer, C., Johnsen, S., Jouzel, J., Kubik, P. W.,  
1176 Lestringuez, J., Stiévenard, M., Suter, M., and Yiou, P.: Beryllium 10 in the Greenland Ice Core Project ice core  
1177 at Summit, Greenland, *J. Geophys. Res. Oceans*, 102, 26783–26794, <https://doi.org/10.1029/97JC01265>, 1997.
- 1178 Zappala, J. C., Baggenstos, D., Gerber, C., Jiang, W., Kennedy, B. M., Lu, Z. T., Masarik, J., Mueller, P.,  
1179 Purtschert, R., and Visser, A.: Atmospheric 81Kr as an Integrator of Cosmic-Ray Flux on the Hundred-  
1180 Thousand-Year Time Scale, *Geophys. Res. Lett.*, 47, e2019GL086381, <https://doi.org/10.1029/2019GL086381>,  
1181 2020.
- 1182 Zhao, X., Cheng, H., Sinha, A., Zhang, H., Baker, J. L., Chen, S., Kong, X., Wang, Y., Edwards, R. L., Ning, Y.,  
1183 and Zhao, J.: A High-Resolution Speleothem Record of Marine Isotope Stage 11 as a Natural Analog to  
1184 Holocene Asian Summer Monsoon Variations, *Geophys. Res. Lett.*, 46, 9949–9957,  
1185 <https://doi.org/https://doi.org/10.1029/2019GL083836>, 2019.
- 1186